doi:10.26443/seismica.v5i2.2506

T-phase detection within spectrograms of hydroacoustic data from the Arctic Ocean

Marianna Anichini * [1,5], **Jonathan Cleverly** [2], **Vår Dundas** [3,5], **Mathilde B. Sørensen** [1], **Philippe Blondel** [2], **Espen Storheim** [3], **Hanne Sagen** [3], **Matthew Dzieciuch** [4]

[1]Department of Earth Science, University of Bergen, Bergen, Norway, [2]Department of Physics, University of Bath, Bath, UK, [3]Nansen Environmental and Remote Sensing Center, Bergen, Norway, [4]Institute of Geophysics and Planetary Physics, Scripps Institution of Oceanography, University of California, San Diego, San Diego, USA, [5]Bjerknes Centre for Climate Research, Bergen, Norway

Author contributions: *Conceptualization*: Anichini. *Methodology*: Anichini, Cleverly. *Software*: Cleverly. *Validation*: Sørensen, Blondel, Storheim. *Formal Analysis*: Anichini, Cleverly. *Investigation*: Anichini, Cleverly. *Writing - Original draft*: Anichini, Cleverly. *Review & Editing*: Anichini, Cleverly, Sørensen, Blondel, Storheim, Sagen, Dzieciuch, Dundas. *Visualization*: Cleverly. *Supervision*: Sørensen, Blondel. *Project administration*: Sørensen. *Data acquisition*: Sagen, Dzieciuch. *Funding acquisition*: Sørensen, Blondel, Sagen, Dzieciuch.

Abstract Microseismicity in the Central Arctic remains understudied due to its remoteness from land seismic stations. Hydrophone arrays can be used to detect earthquakes from their T-phases, components that propagate in water. This approach can provide a valuable alternative to traditional recording systems and improve the monitoring coverage. However, manual annotation of T-phases are a time-consuming process, and more automated approaches are needed. Recent studies in T-phase detection consider machine learning techniques, but these methods are computationally intensive and sensitive to training data. In this study, an automated detector is presented utilising a Regions Of Interest (ROI) algorithm on spectrograms, requiring minimal parameter tuning and computational resources. The detector was applied to acoustic data recorded along the Nansen Basin from September 2019 to August 2020 during the CAATEX experiment. The ROI detector correctly identified 82 out of 96 manually labelled earthquake events across all moorings, with the majority of false detections linked to the presence of flow noise within hydrophones. The algorithm also characterised spectro-temporal properties of T-phase signals, with energy focused between 3 and 50 Hz, peaking at around 20 Hz. This method is robust against the varying underwater background noise conditions encountered and aids in studying the complexities of the T-phase signal structure.

Production Editor: Gareth Funning
Handling Editor: Kenneth Macpherson
Copy & Layout Editor: Ethan Williams

Signed reviewer(s): Sara Bazin

Received: January 20, 2026
Accepted: September 5, 2026
Published: October 21, 2026

1 Introduction

Monitoring seismic activity in the Arctic Ocean is logistically difficult. Persistent ice cover in the Arctic Ocean presents challenges for the deployment and recovery of ocean-bottom seismometers (OBS), which are traditionally used to record microseismicity (Kong et al., 1992; Wolfe et al., 1995; Sohn and Hildebrand, 2001; Jeddi et al., 2021). OBSs are small enough that they can drift with ocean currents during ascent to the surface, potentially over greater distances than in conventional deployments (Schlindwein et al., 2025). Consequently, the recovery location ('pop-up site') can be considerably displaced from the original deployment position (Schlindwein et al., 2025). In such environments, hydrophones placed on large mooring systems may therefore represent an alternative approach for monitoring seismic activity, as the moorings are generally easier to relocate and recover than free-rising instruments. Hydrophone arrays have been successfully used (mainly at mid-latitudes) as alternative tools for long-term deployments to reduce the monitoring gap in remote ocean areas, where only the larger events are detected by land-based seismic networks (Fox et al., 2001; Bohnenstiehl et al., 2002; Dziak et al., 2004; Williams et al., 2006; Parnell-Turner et al., 2022; Ingale et al., 2023, 2025).

Earthquakes contribute to the ocean's soundscape (Hildebrand, 2009; Schwardt et al., 2022; Ainslie et al., 2025). Part of the seismic energy generated within the oceanic crust can be released as hydroacoustic signals into the water column, as T-phases, or tertiary waves (Tolstoy and Ewing, 1950). In the current study, the term T-phase is used broadly to describe any clearly hydroacoustic earthquake signal, generated at the crust-water interface (source), travelling in water (path) and recorded by a hydrophone (receiver). Importantly, the T-phase generation can occur through different conversion mechanisms. In the slope-generated mechanism, seismic rays propagating through the crust intersect steep bathymetric features, such as continental slopes, or seamounts, and part of their energy is converted into hydroacoustic waves generating slope T-phases (Williams et al., 2006; Talandier and Okal, 1998). Alternatively, in abyssal environments, seismic rays travelling through the crust may reach rough or irregular seafloor topography, where scattering and mode conversion at the crust-water interface generate hydroacoustic energy, producing abyssal T-phases (Park et al., 2001; de Groot-Hedlin and Orcutt, 1999; de Groot-

*Corresponding author: marianna.anichini@uib.no

Hedlin and Orcutt, 2001; Walker et al., 1992; Yang and Forsyth, 2003).

Although the T-phase is the most common seismic signal recorded by hydrophones (Dziak et al., 2004; Guilbert et al., 2005; Ingale et al., 2025), direct arrivals of body seismic phases (P and S) can also observable in hydroacoustic data, particularly for events occurring close to the receiver (distance < 200 km) or at high enough magnitude (Dziak et al., 2004; Goslin et al., 2012). P- and S-phases can be easily discriminated by their lower amplitudes, shorter durations and earlier arrival times, as T-phases experience a lower velocity propagating through water (Blackman et al., 2000; Dziak et al., 2004; Sukhovich et al., 2014; Garibbo, 2023). Generally, T-phase signals can last from a few seconds up to several minutes, appearing as a sustained signal with both an amplitude and spectral envelope, the onset of which is typically shorter than the tail-off (Tolstoy and Ewing, 1950; Schreiner et al., 1995; Okal, 2008; Tolstoy and Bohnenstiehl, 2005). Whilst the majority of energy of T-phases is centred between 5 and 20 Hz, significant energy can be carried at higher frequencies, even beyond 100 Hz (Bohnenstiehl et al., 2002; Oliveira et al., 2025). Body phases are unable to retain these high frequency components during propagation to the same extent as T-phases, due to the crust's attenuative properties compared to water (Fox et al., 2001; Okal, 2008). The temporal and spectral characteristics of T-phases are partly determined by seismoacoustic coupling at the crust–ocean interface (Okal, 2008; Jamet et al., 2013), but also by the properties of the oceanic waters. The latter can affect the T-phase path and allow for optimal acoustic propagation, such that even earthquakes of moderate magnitudes (M_w < 4), can be detected thousands of kilometres away from their epicentres (Williams et al., 2006; Okal, 2008; Ingale et al., 2021).

Across mid-latitude oceans, the minimum sound velocity is typically located around 800-1,200 m depth, forming the SOFAR channel (SOund Fixing And Ranging), allowing for efficient long-range acoustic propagation (Munk et al., 1995). In the Arctic Ocean (> 70°N), the stratified water column (Sec. S6) results in a near-surface sound speed minimum (Diachok, 1976; Sagen et al., 2016, 2017; Dundas et al., 2026), in turn leading to a 'surface duct' for optimal transmission of sounds below 50 Hz, which includes the majority of acoustic energy of T-phases (Okal, 2008; Fox et al., 2001). The duct can extend to depths of around 1,000 m (Buckingham, 1991), so once sound has upwardly refracted towards this duct, it will experience few ocean bottom interactions (limited to ridges and continental slopes) but will scatter from the rough underside of sea ice (Diachok, 1976; Keenan and Merriam, 1990).

Consequently, as T-phases can be received far from the seismoacoustic coupling region, they have been the focus of numerous empirical studies with diverse applications: investigating earthquake source properties and oceanic upper mantle structure (de Groot-Hedlin and Orcutt, 2001; Dziak et al., 2004; de Melo et al., 2021); monitoring underwater volcanic eruptions and their processes (Talandier and Okal, 1987; Fox and Dziak, 1998; Bazin et al., 2022; Saurel et al., 2022; Lavayssière et al., 2024; Guilbert et al., 2005) and expanding tsunami warning systems (Takemura et al., 2024). In contrast to the previous works, mainly performed at temperate latitudes, there have been few studies of T-phases in the Central Arctic, and, as such, there are still many unknowns about their generation and propagation mechanisms in the region (Blackman et al., 2000; Sohn and Hildebrand, 2001; Schlindwein et al., 2005). T-phases from microseismic events in the region may hold crucial information for better understanding seismic activity along the Gakkel Ridge, one of the slowest-spreading mid-ocean ridges on Earth (Sohn and Hildebrand, 2001; Schlindwein et al., 2007; Koulakov et al., 2022).

For spaced hydrophone networks, detection of T-phases relies on human experts who visually inspect large acoustic datasets and manually annotate target signals (Fox et al., 2001; Ingale et al., 2021). Although this labelling approach is widely adopted, it can be subjective and time-consuming due to the large volumes of data generated by continuous recordings (Sukhovich et al., 2014; Vaezi and van der Baan, 2015; Raumer et al., 2024b). Recent methods for detecting T-phase signals in hydrophone data have utilised Machine Learning (ML, Sukhovich et al., 2014; Raumer et al., 2024b); however, they may still be biased to only detect seismic signals with features similar to those used to train the model.

Therefore, there is still a need to improve tools for automatic file processing and T-phase signal detection, with simpler parameter settings and higher robustness to variable noise conditions. The present work aims to address this, proposing a new signal-detection method for T-phases in hydroacoustic data. Spectrograms are used to explore seismic activity and delineate both temporal and spectral characteristics of T-phase events. The adaptability of the method has been tested using data from hydrophone deployments in the Nansen Basin, where soundscape contributions from wind, waves, cryophony (sounds from sea ice processes) and biophony (mainly marine mammal vocalisations) can vary significantly, both seasonally and hourly, allowing for the detector to be trialled against a range of noise conditions.

2 Background

In seismology, detection triggers typically operate in the time and frequency domains, employing template matching or analysing signal envelopes and amplitudes (Withers et al., 1998; Vaezi and van der Baan, 2015). These methods require rigorous fine-tuning of several parameters to accommodate the noise and signal characteristics of specific seismic regions. The Short-Term-Average/Long-Term-Average (STA/LTA, Allen, 1978), a widely used approach, exemplifies this challenge. Its threshold setting presents a fundamental trade-off. Set too high, it may miss weak events (False Negatives). Set too low, and it may generate an excessive number of irrelevant triggers (False Positives) (Vaezi and van der Baan, 2015). This sensitivity-specificity characteristic reflects a broader limitation in seismic trigger algorithms: weak events often remain undetected

when signal-to-noise ratio thresholds are set too conservatively (Vaezi and van der Baan, 2015). Among the alternative automatic detection methods for seismic signals, Matsumoto et al. (2006) presented an adaptive-threshold approach specifically for T-phase detection, combining simple signal processing with adaptive noise thresholds. Despite its dynamic adaptation to changing noise levels, the method exhibits high False Positive rates, suggesting that further refinement is needed to monitor seismic activity across diverse underwater soundscapes with higher accuracy.

Previous papers presenting ML techniques for identifying and categorising geophonic signals against other sounds in hydrophone data have been published (Sukhovich et al., 2014; Raumer et al., 2024b). While the outcomes of these methods are promising, they still lack universality in their applications. For instance, in the method proposed by Sukhovich et al. (2014), the training datasets included only four signal types (T waves, teleseismic P waves, ship-generated sound, and iceberg-generated sound), likely limiting its applicability to more diverse environmental noise conditions. Moreover, the method proposed by Raumer et al. (2024b) does not explore in detail the types of seismic signals detected, with their benchmark focusing mainly on binary classification tasks. This aspect may reflect that trained models may not generalise well to different underwater noise conditions or signal types (e.g. various T-phase spectral appearances) without further adaptation.

The detection method proposed in the current study uses the Regions Of Interest (ROI) algorithm, whereby image processing techniques are applied to spectrograms to locate individual acoustic signatures (Ulloa et al., 2021). The methodology is modular in its processing steps, allowing for techniques to be easily swapped at the various stages (e.g. noise removal). The processing presented here is intentionally minimalist to allow the algorithm to run with few input parameters and be suitable for limited computing resources. ROI algorithms have not seen much use as a stand-alone detector. They have been applied in conjunction with machine learning techniques to detect and categorise specific groups of sounds, such as calls of marine mammal species (Thode et al., 2012; Escobar-Amado et al., 2022). Other studies have shown that ROI algorithms can be used to highlight periods of increased vocal activity (Cleverly et al., 2024), although difficulties were encountered in detecting overlapping sounds separately and handling sounds of varying amplitudes. The ROI algorithm has yet to be applied explicitly to geophonic signals. T-phases appear distinctively on spectrograms; therefore, the algorithm can be designed to focus solely on detecting these events, whilst ignoring other sounds.

The ROI algorithm described is used as an automatic tool for logging earthquake events across large spectrogram datasets. While spectro-temporal properties are collected for every earthquake found, the technique is currently not suitable for phase-time picking. As such, 'detection' refers to an event in the spectrogram that has been recognised by the algorithm as a ROI; confirmation of the event being geophonic was completed manually, along with determining phase type.

3 Materials and Methodologies

3.1 Acoustic data collection and processing

The Coordinated Arctic Acoustic Thermometry Experiment (CAATEX) deployed three multi-sensor moorings (NERSC1-3) in the Nansen Basin (Dzieciuch et al., 2022, 2026) (Figure 1). Across the moorings, hydrophones were synchronised to record every 12 hours for 45 minutes and 12 seconds, with a sample rate of 976 Hz. One hydrophone at a depth within 1,000 to 1,050 m was selected from each mooring to study seismic activity. From this depth, noise from sources at the sea surface is reduced, allowing for better conditions for studying weak seismic signals. A low-frequency (< 50 Hz) continuous M-sequence signal was transmitted from NERSC1 every 3 days to conduct thermometry measurements. Due to both its high Received Level and rich harmonic content, the parts of the recording containing this signal were removed from analyses (this corresponds to the first 17 minutes of a recording, when the transmission was scheduled). All recordings were written to lossless Waveform Audio File Format (.wav) with the following hydrophone calibration: a receiving sensitivity of -168 dB re 1 V/µPa, a pre-amplifier gain of 12 dB and an analogue-to-digital conversion voltage of 2.5 V. During the recording of data, a high-pass filter, with a cut-off frequency at 7 Hz and an unrecorded roll-off, was applied at each hydrophone, such that power levels below 7 Hz cannot be accurately determined. For simplicity, the hydrophone calibration was assumed to be consistent across the entire frequency range available. The dataset analysed in the current study included 1,967 files (656 from each hydrophone - except NERSC3 that had 655 files) collected from 3rd September 2019 (11:59:50) to 26th July 2020 (11:59:50).

Power Spectral Density (PSD) spectrograms were used throughout this study, computed by dividing the waveform into 2 s segments with 50% overlap and convolving with a Hann window function, following guidelines from Merchant et al. (2015). With this setup, spectrograms had temporal and spectral resolutions of 1 s and 0.5 Hz, which were sufficient to capture finer details of seismic signals along both axes.

3.2 Manual detection dataset and event quality determination

Recordings from NERSC1 were visually inspected by an expert annotator (MA) using the Triton software package (v.1.92, Wiggins et al. 2010) in MATLAB (Version R2018b). Earthquake signals were observed and manually labelled in spectrograms with a frequency range of 0.5 to 300 Hz. Each seismic event was labelled chronologically with a timestamp and attributed a unique 'Event ID'. The visible seismic phases, either P- and T-phases together ('P_T') or just the T-phases by themselves ('T'), have been assigned to each event. Events were separated into three categories based on signal quality: 'Strong', 'Medium' or 'Weak', presented

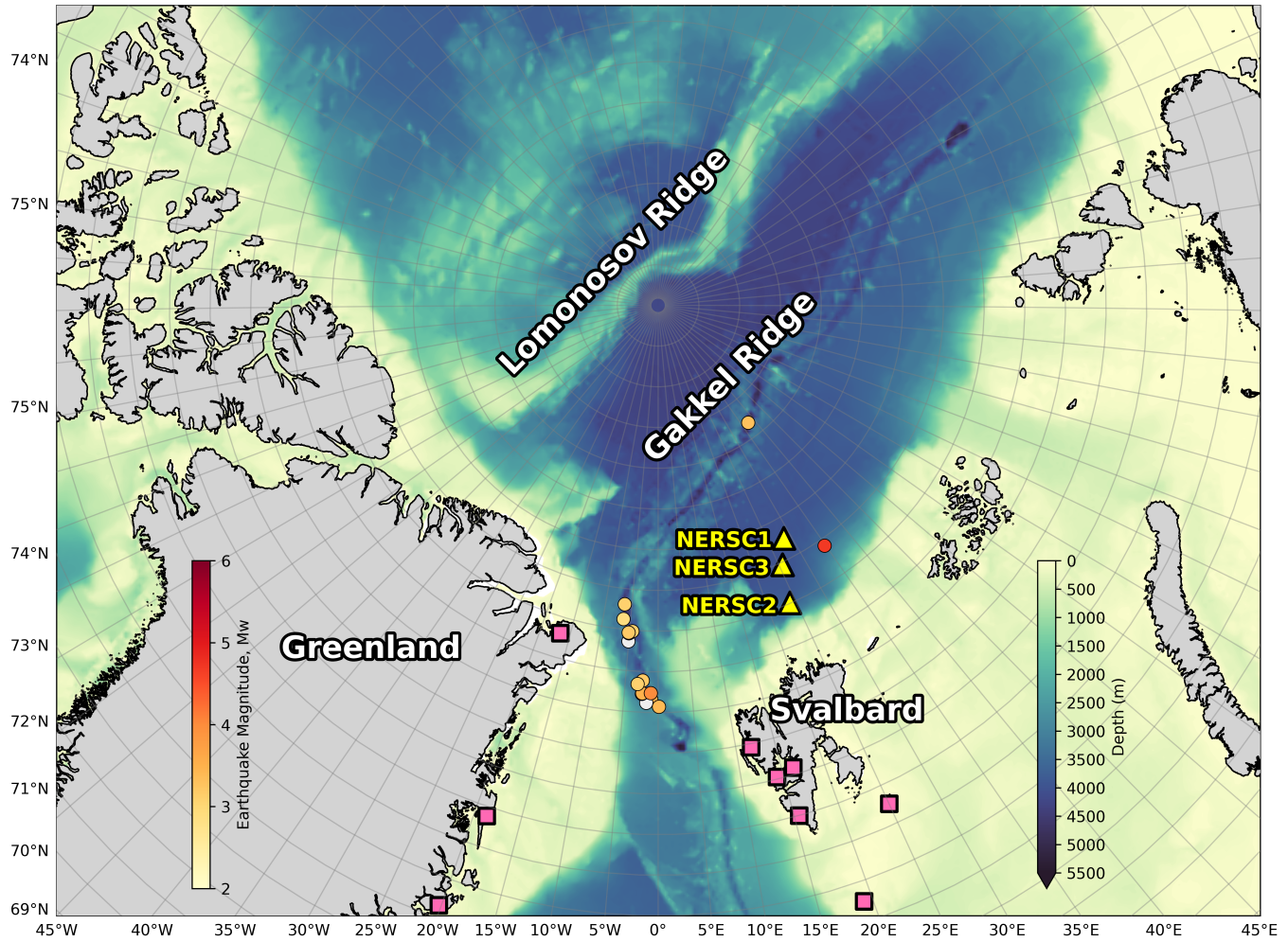


Figure 1 Map presenting the region of study and locations of CAATEX moorings (NERSC1-3, yellow triangles). Earthquakes recorded between 2019 and 2020 are presented, located by land stations of the Norwegian National Seismic Network (NNSN, pink squares) and reported by the International Seismological Centre (ISC) (circles). Only those that occurred whilst hydrophones were actively recording are included in the plot (16 in total). The magnitude (M_w) of these events is indicated by a colour scale (grey for missing M_w values). Five events have been found in both land stations (NNSN) and hydroacoustic data (CAATEX): one located in the Gakkel Ridge, one located on the right side of the moorings, and three located in the Fram Strait (more details in Table S2). Bathymetry data were sourced from the IBCAO v5 2025 400 m grid. (Jakobssen et al., 2024).

in Figure 2. The quality categories were based on two primary criteria: signal clarity (how visible the start and end of signals were in the spectrogram) and amplitude characteristics. Strong signals displayed both higher amplitudes and clear temporal evolution throughout the seismic event (Fig. 2a-b). Medium quality signals were clearly defined in time, but with relative amplitudes lower than the strong category (Fig. 2c). Weak signals were characterised by poorly defined start and end times (Fig. 2d). The presence of each event was visually checked and compared across all three hydrophones, with different quality labels given to the T-phase signal depending on the criteria described above. Thus, some events were assigned different quality categories between moorings.

Mean PSD spectra were plotted to enhance the difference in amplitude of events classified within the three quality categories (Fig. S1). From this analysis, the mean PSD values of weak, medium and strong events significantly differed in 5 dB re 1 $\mu Pa^2/Hz$ within the frequency range seismic sounds occupy. Finally, to test the detector algorithm, the event dataset has been created and included Event ID, phase type, quality, corresponding .wav file name, mooring name, and date and start time of the annotation.

3.3 Computation of Regions Of Interest (ROI)

The spectrogram representation of a signal can be treated as an image, where each time step-frequency bin pairing (referred to as 'bin') is equivalent to a pixel. By combining multiple image processing techniques, detectors for acoustic signatures can be designed, analogous to object detection within images. The ROI algorithm considered in the present study is based on the double-threshold hysteresis method for edge detection in images, first described by Canny (1986). To identify ROIs, two thresholds are initially applied to the spectrogram. The first finds the local maxima along the spectrogram (bins with amplitude values greater than the threshold), while the second is used to collect bins around the maxima to form the outline of the signatures

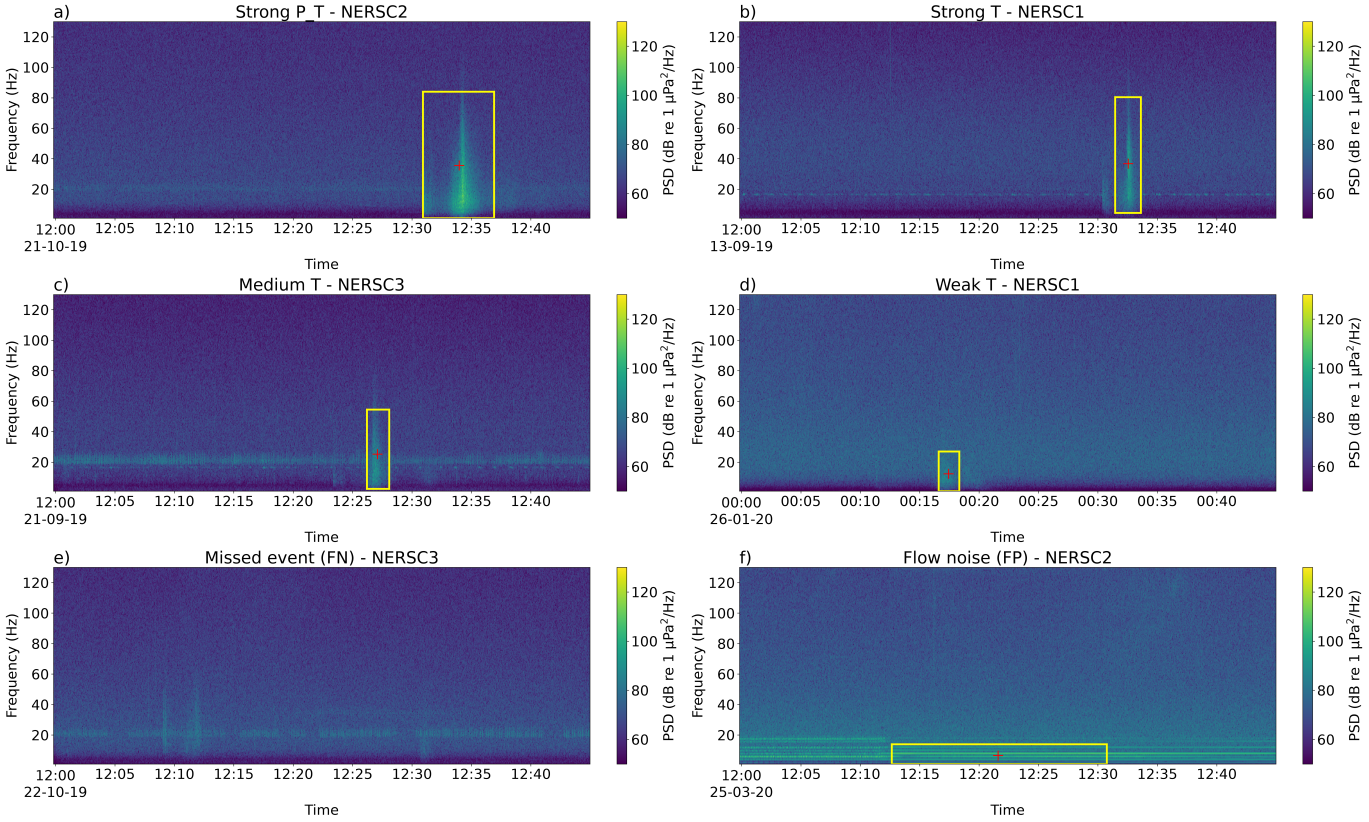


Figure 2 Comparison of different earthquake signal qualities and phase types discussed: a) Strong P_T-phase; b) Strong T-Phase (note the presence of an undetected P-phase just before the detected T-phase); c) Medium T-Phase; d) Weak T-Phase; e) Missed event at 12:10 (False Negative, FN); f) Flow noise (False Positive, FP). These detections were made using the ROI algorithm, discussed in Section 3.3 and subsequent sections, with the yellow boxes and red crosses representing the temporal bounds and centroid of the ROI computed. Spectrograms were computed using code derived from PAMGuide (Merchant et al., 2015) and PAM2Py (Rodríguez et al., 2021).

in the spectrogram. Afterwards, a binarisation mask (assigning bins the value '0' if they lie outside an ROI, then '1', '2', '3' etc. within ROIs) is applied to the spectrogram to separate acoustic signatures into individually labelled ROIs (Shapiro, 1996). This approach is implemented in the *rois* module of *scikit-maad*, a Python package for quantitative soundscape analysis (Ulloa et al., 2021), which was adapted in the current work for detecting seismic activity.

The processing stages of the ROI algorithm are presented as a set of spectrograms in Figure 3. A seismic event recorded from NERSC1 served as an example of a detected target (Fig. 3a). Modifications were made to the pre-processing stages of the ROI algorithm in *scikit-maad.rois*. The default median equaliser, which balances low-amplitude bins to the median level, was replaced with a median threshold, where bins with an amplitude less than or equal to the median level (along the frequency axis) were dropped to the minimum level of the spectrogram (Fig. 3b). Next, a Gaussian filter was applied to the spectrogram (Fig. 3c), with a standard deviation of 5 bins (kernel size); 5 s along the time axis, 2.5 Hz along the frequency axis. The filter is primarily used to smooth the spectrogram, allowing finer details of seismic event signatures to couple together, improving the prominence of the event. The selection of the filter kernel size was wider than what is typically recommended in *scikit-maad.rois* (between 0.5 to 3 bins), to suppress any non-seismic sounds of shorter duration or narrower bandwidth that may have been present in the spectrogram (e.g. whale calls). T-phase signals featuring both short durations (< 5 s) and narrow bandwidth may get suppressed partly by the Gaussian filter, but given that the bandwidths are typically wider than the kernel size along the frequency axis, these signals would not be erased entirely. Additionally, the choice in kernel size further reduced background noise, enabling the use of lower amplitude thresholds of 75 and 60 dB re 1 µPa^2/Hz for locating ROIs within the spectrogram (Fig. 3d).

The ROI algorithm has a few drawbacks preventing it from being used as an arrival time picker for an earthquake location. When computing spectrograms, a compromise needs to be made between preserving temporal and spectral resolutions. As such, the 1 s temporal resolution used in this study (Sec. 3.1) is insufficient for comparing arrival times of an earthquake signal between hydrophones to determine its origin, but it allowed for an improved spectral resolution of 0.5 Hz for studying spectral characteristics of earthquakes. While the algorithm was tuned to detect individual T-phase signals, if the P- phases were observable in the spectrogram, they could merge with the T-phase to form a single, extended ROI during the binarisation masking stage (resulting from amplitude being smoothed by the Gaussian filter between the two phase signatures), which is

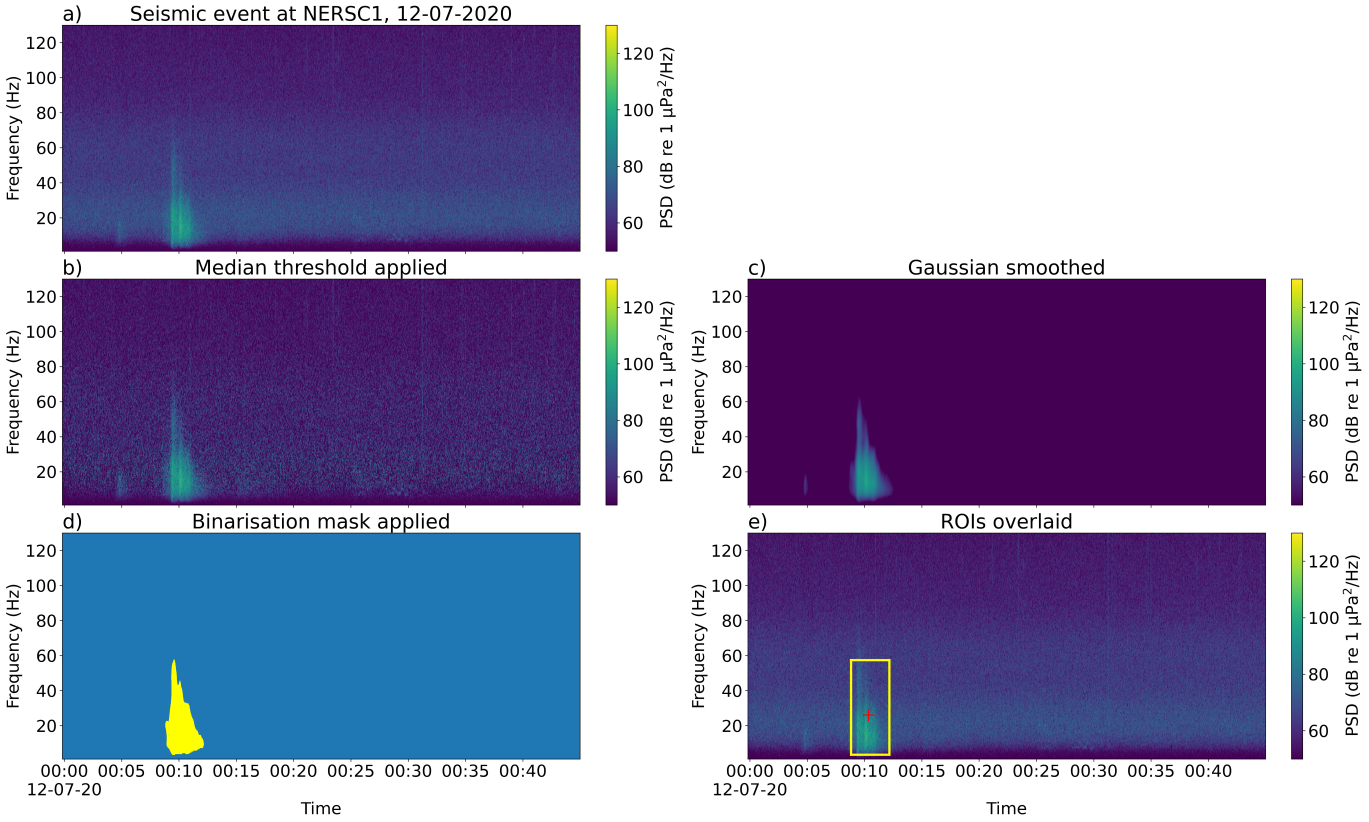


Figure 3 Processing stages for computing ROIs within a spectrogram, using a seismic event recorded at NERSC1 (on 12th July 2020) as an example target. a) Original spectrogram. b) Application of median threshold. c) Smoothing using a Gaussian filter. d) Applying the binary mask, highlighting regions within the spectrogram captured by the double threshold. e) Spectro-temporal bounds (yellow box) and centroid (red cross) of the ROI captured.

not optimal for automated time of arrival calculations, particularly if there were differences in which phases were detected between hydrophones.

Computation of ROIs was limited between 1 and 130 Hz, covering the typical frequency range for seismic signals, with an extended upper frequency limit to accommodate potential variations (Williams et al., 2006; Garibbo, 2023). A set of acoustic features for the extent and centroid of each computed ROI (Fig. 3e) were written to file: start time, end time and duration (t_{start}, t_{end}, T), minimum and maximum frequency and bandwidth (f_{min}, f_{max}, Δf), temporal centroid (t_c, from t_{start}), spectral centroid (f_c) and time-frequency area (A_{tf}, i.e. $T \times \Delta f$). Only ROIs with $f_c < 60$ Hz were counted for analyses, as there were occasions where sudden increased background noise or impulsive sounds would merge into sizeable ROIs, centred above 60 Hz and clearly not associated with seismic activity (Fig. S9). ROIs with an area $\leq$ 25 bins^2 were not counted as ROIs (a default filter in *scikit-maad.rois*), although the majority of these would be removed from the spectrogram during the Gaussian smoothing stage.

Using a computer of modest performance (Lenovo ThinkPad L14 Gen 3 with 12th Gen Intel® Core™ i7-1255U, 1700 MHz, 10 cores, 2 logical processors, 16 GB physical RAM), processing of a single 45-min recording to compute both its spectrogram and the ROIs within it would take between 10 to 20 seconds. The number of ROIs computed within the spectrogram did not affect speed significantly.

3.4 Statistical analyses

ROIs were computed across the CAATEX hydrophone dataset, then compared to the manually-annotated dataset, determining the number of True Positives, seismic signals captured by the detector ('TP' in figures and tables); False Positives, non-seismic activity captured by the detector ('FP'); and False Negatives, seismic signals recorded in the manual catalogue but not captured by the detector ('FN'). Signals were counted separately between hydrophones, such that if seismic signals from a single earthquake event were identified as ROIs across all hydrophones, that would equate to three True Positives. A False Negative would be counted for a missed annotated T-phase signal at one hydrophone (Fig. 2e), regardless of whether the event was captured at another hydrophone. ROIs clearly associated with seismic activity but not corresponding to an entry in the manual catalogue were still labelled as a True Positive and referred to as 'new seismic activity' in subsequent sections ('TP_{new}'). The number of True Negatives ('TN') was not determined, as they would constitute all non-seismic sounds in the hydrophone recordings along with background noise, which cannot be discretely defined in the spectrogram. Performance was assessed using the standard metrics used for classification tasks, precision and

recall, given by the equations,

$$\text{Precision} = \frac{TP + TP_{new}}{TP + TP_{new} + FP} \quad (1)$$

$$\text{and} \quad \text{Recall} = \frac{TP}{TP + FN}. \quad (2)$$

Specifically, precision refers to the percentage of ROIs attributable to seismic events, whereas recall refers to the percentage of events in the manual catalogue captured by the ROI detector.

Principal Component Analysis (PCA) was used to determine which acoustic features (Sec. 3.3) were best at characterising seismic signals. This is a common approach for dimensionality reduction, selected to reduce the acoustic features into a set of independent 'Principal Components' ('PCs', Jolliffe and Cadima 2016; Greenacre et al. 2022), explaining the underlying variance in the dataset. Correlation scores between features and Principal Components highlight which features contribute most to the variance (high correlation scores with PC_1), and which are redundant (low correlation scores with the first few PCs). From this, correlations between individual acoustic features were made, along with observing how well separated True Positive detections were from False Positives. All acoustic features were included in these analyses, except for t_{start} and t_{end}.

PSD spectra within the computed ROIs were compared to background noise from their corresponding recordings to assess the performance of the detector under different noise conditions. The 95th-percentile PSD spectra, representing maximal energy (Merchant et al., 2015), were computed for individual ROIs within their temporal bounds, and then for each recording, with ROI sections removed. With this, periods of increased background noise can be observed, as they were deemed potential obstacles for the performance of the detector. Maximum Received Level (RL_{max}) was also measured for each ROI associated with seismic activity, i.e., TP and TP_{new}, by measuring Broadband Sound Pressure Level within the spectro-temporal bounds of the ROI. These RL_{max} values were then compared to the signal qualities determined during the manual annotation of the dataset.

4 Results

4.1 Detection performance: from manual dataset to detections with ROIs

A total of 1,968 files, corresponding to 1,476 hours of recording time, were processed both manually and automatically. To evaluate the algorithm's performance on seismic activity, the ROI detections were compared to the earthquakes reported in the manual dataset. Out of the 96 labelled earthquake events, 82 (85%) were detected as True Positives within at least one of the hydrophone recordings by the ROI algorithm (Fig. 4). For the remaining undetected 14 events, 11 were categorised as False Negatives (11%) between all three hydrophones, whereas 3 (3%) could not be processed (Tab. 1; Fig. 4). Event 53 was not detected due to the spectro-temporal bounds of the ROI capturing it together with Event 52. Events 27 and 43 were concurrent with omitted parts of the recording (due to the thermometry signal), whereas Event 78 at NERSC3 was missing due to the lack of a file at this time. There were 6 occurrences of an earthquake signal being present at both NERSC1 and NERSC3, but absent at NERSC2 (Events 35, 42, 49, 58, 69 and 94), i.e., unobservable when manually inspecting spectrograms. These missing earthquake signals at NERSC2 are referred to as 'Absent' signals hereinafter.

The majority of phase types attributed to signals in the manual dataset were in agreement with what was detected by the ROI algorithm. Using both detection methods, manual and ROI, the most representative phase type among True Positives was T, especially in medium and weak quality signals (Tab. 1; Fig. 2c-d). In the manual dataset, more P_T signals were labelled in comparison with the ROI detections, although the presence of P_T was highest in Strong signals. The highest discrepancy between ROI and manual labels was found with P_T signals, independent of signal quality and mooring (Tab. 1). A total of 22 signals were noted as having both P- and T-phases in the manual dataset, but with only the T-phase detected as an ROI. There were 10 P_T signals where the P-phase was detected as a separate ROI. These P-phase detections were omitted from the rest of the statistical analyses.

4.2 Detection performance: event detection between hydrophone moorings

Out of the 342 ROIs computed across the CAATEX dataset (excluding the aforementioned 10 P-phase ROIs), 201 were associated with T-phase signals labelled in the manual dataset. After completing comparisons with the manual dataset, the remaining ROIs were manually inspected and categorised: 100 were associated with non-seismic sounds, hence labelled as False Positives; and 41 were determined to be seismic related and, hence, labelled as 'new seismic activity' (Sec. 3.4). Among these, 7 occurred in temporal proximity to previously labelled T-phase signals (i.e., within the same recording). It is therefore unclear whether they represent T-phases generated by a distinct new signal or a secondary signature of an annotated T-phase signal. For the present analysis, these 7 ROIs are treated as separate T-phase signals.

Overall, the detector had a precision of 71% and a recall of 74%, as shown in Table 2. However, the performance varied significantly across the three selected hydrophones in terms of True Positives (TP), False Positives (FP), False Negatives (FN), newly discovered seismic signals and absent signals. Highest precision was achieved at NERSC1, with 92% of the ROIs computed being associated with either known or new seismic signals. At NERSC3, 76% of ROIs were seismic signals, since there was a notable increase in False Positives, lowering the precision of the detector at this hydrophone. Precision was much lower at NERSC2, with only 53% of ROIs being seismic signals. Absent signals were only reported in NERSC2 (Tab. 2; Fig. 4). The high-

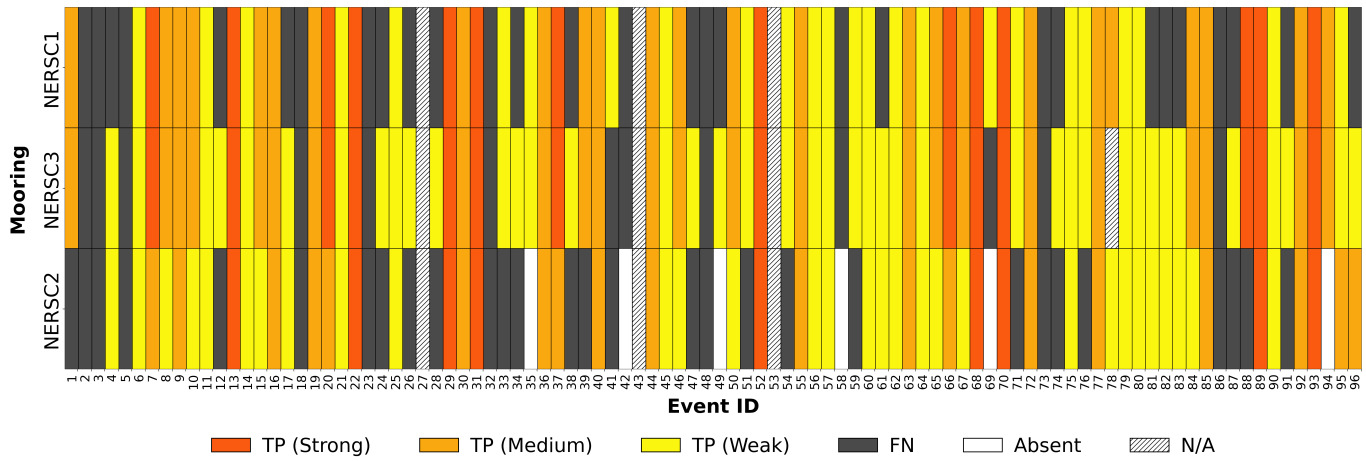


Figure 4 Summary of events logged in the manual dataset (x-axis) compared to what was detected by the ROI algorithm at each mooring (y-axis). Moorings are listed from north (top) to south (bottom). True Positive (TP) occurrences are separated by quality labels: Strong (dark orange), Medium (light orange) and Weak (yellow), alongside False Negative (FN) occurrences (dark grey). 'Absent' (white) refers to occasions where an earthquake signal was not observable at that particular hydrophone (by eye when inspecting the spectrogram) but was observable from other hydrophones. 'N/A' (hatched) refers to occasions where an event at a particular hydrophone could not be processed.

Mooring	Quality	Manual T	Manual P_T	Auto T	Auto P_T	Total True Positives
NERSC1	Weak	22	3	25	0	25
NERSC3	Weak	34	7	39	2	41
NERSC2	Weak	24	6	29	1	30
NERSC1	Medium	16	9	24	1	25
NERSC3	Medium	17	7	23	1	24
NERSC2	Medium	14	5	17	2	19
NERSC1	Strong	1	13	6	8	14
NERSC3	Strong	0	14	8	6	14
NERSC2	Strong	2	7	5	4	9

Table 1 Comparison between manual earthquake signal annotations and True Positive detections by the ROI algorithm, counted per hydrophone mooring and quality. Manual T: signals manually labelled where only the T-phase was present, Manual P_T: signals manually labelled where both the P- and T- phases were present, Auto T: ROI detections comprising only the T phase, and Auto P_T: ROI detections comprising the P- and T- phases combined; Total True Positives: total number of True Positive signals found in both the manual dataset and by the ROI algorithm.

est recall of manually annotated seismic signals was achieved at NERSC3, with 86% of the known signals captured, whereas NERSC1 and NERSC2 had similar performance in this aspect, recalling 69% and 67%, respectively (Tab. 2; Fig. 4). Regarding newly discovered seismic signals, NERSC3 had the highest count, followed by NERSC2 and then the fewest new signals at NERSC1 (Tab. 2).

In terms of phase types and signal quality, True Positives were mainly represented by Weak T-phase signals at all hydrophones except NERSC1, which had the same number of detections in the Medium quality category (Fig. 4; Tab. 1). NERSC2 recorded the fewest number of T-phase signals of Medium quality, while NERSC3 had the highest. Lastly, the highest number of strong P_T signals was captured at NERSC1. The vast majority of False Negatives were Weak T-phase signals, but there were some outlying signal types missed: two Weak P_T phase signals (one from NERSC1 and NERSC2 each) and one Medium quality T-phase signal (NERSC2). The majority of newly discovered seismic signals were represented by just the T-phase, although there was one instance of both the P- and T-phases being combined into one ROI along NERSC2. Signal qualities were not assigned to these new signals, but they were largely comparable to Weak annotated signals detected.

4.3 Variance of acoustic features

Findings from performing PCA on the ROI acoustic features (from all hydrophones) are presented in Figure 5. More than 90% of the variance within the dataset was explained by the first three components ('PCs'), 45.8% of which was explained by PC_1 alone (Fig. 5a). The features f_{max}, Δf and f_c positively correlate and had comparable scores of around 0.5 for PC_1 (Fig. 5b), while low scores were found for the remaining features, with only slight positive influence from A_{tf} and f_{min}. A slight negative contribution came from T and t_c. In turn, PC_2 accounted for 33.2% of explained variance within the

Mooring	TP	FP	FN	TP_{new}	Absent	Precision (%)	Recall (%)
NERSC1	64	6	29	9	0	92	69
NERSC3	79	31	13	19	0	76	86
NERSC2	58	63	29	13	6	53	67
Total	201	100	71	41	6	71	74

Table 2 ROI classification counts (including 'Absent' signals, i.e. signals that were not observed at that particular hydrophone, but were observable at other hydrophones), precision and recall per mooring. The 10 ROIs associated with P-phases have been excluded from this count.

acoustic features, with T, t_c and A_{tf} correlating significantly and positively (scores around 0.5) (Fig. 5c), whereas f_{min} had a less significant negative correlation with the component. Other spectral features had negligible influence on PC_2. Finally, 12.2% of the variance in the dataset was explained by PC_3, with f_{min} strongly correlating positively with the component, and with minor positive influences from T, t_c, and a minor negative influence from Δf (Fig. 5d).

As seen in the projection of PC_1 against PC_2 in Figure 5e, most True Positives were clustered towards the origin of the PC_1-PC_2 projection, highlighting a level of uniformity between True Positive detections. Outlying True Positives in the positive PC_1-positive PC_2 space were all P_T signals, which ended up having a wider A_{tf} and longer T from the phases coupling into one ROI (presented in Figure S2 in the Supplementary material). Newly detected seismic signals were mostly found in the negative PC_1-negative PC_2 space, indicating that they generally had lower f_{min}, narrow Δf and short T (Fig. 5e). Among these new seismic signals, there were two anomalies, most notably the one far into negative PC_1-positive PC_2 space, suggesting an extended T, and the one far into the positive PC_1 space, alluding to a wide Δf and higher f_{max} and f_c. The latter of these two examples is also the only occurrence where a ROI of new seismic activity combined the P-phase of the T-phase signal of a seismic event. Conversely, False Positives were largely scattered away from the origin of the projection, meaning that their acoustic features deviate significantly from the means of the dataset (Fig. 5e). Many False Positives congregate in the negative PC_1 space, indicating that they predominantly occupy the lower frequencies. Several False Positives spread out along the positive PC_2 direction as well, suggesting increases in T and t_c were common (Fig. 5e).

4.4 Distribution of key acoustic features in the ROIs

Distributions of key acoustic features are presented as histograms in Figure 6. True Positive signals were characterised by T under 200 seconds (Fig. 6a), f_{max} around 50 Hz (Fig. 6b), and Δf between 20 and 60 Hz (Fig. 6c). Similarly, f_c values averaged around 25 Hz. Finally, A_{tf} was generally below 20,000 s Hz (Fig. S3). Newly discovered seismic signals were mainly defined by a reduced Δf and lower f_{max} and f_c (Fig. 6b-d), although the distribution of T was comparable to that of True Positive signals (Fig. 6a). The reduced spectral properties of these newly discovered signals are comparable to the weak True Positive signals. As previously seen in the PCA projection, there was a notable outlier among the newly discovered signals, which features a wide Δf, nearly 120 Hz, and correspondingly increased f_{max} and f_c, suggesting a stronger seismic signal that was missed during the manual annotation process. For the False Positive detections, values of T followed a similar distribution to what was observed for True Positives, although some detections had longer T (up to 1,600 s; Fig. 6a). Additionally, a different pattern was found in the distribution of False Positive spectral values. Although these were still distributed in the low ranges, they had f_{max} and Δf maximum values lower than what was found for True Positives (around 10 Hz and between 1 and 20 Hz, respectively; Fig. 6b, c). Also, the f_c resulted below 15 Hz, well separated from the one characterising the True Positives (Fig. 6d). Lastly, True and False Positive A_{tf} values did not significantly diverge (Fig. S3).

4.5 Influence of background noise on seismic event detection

Levels of background noise varied throughout the deployment of the three hydrophone moorings, as shown in Figure 7. Notably, the high-pass filter applied in the original recording has suppressed ambient noise below 7 Hz (Sec. 3.1); as such, the PSD values presented at lower frequencies do not reflect the natural sonic environment. Noise levels generally increased during the winter period (late October 2019 to mid-May 2020; Fig. 7a, c and e), when wind-sea ice interaction is known to influence the soundscapes to a greater extent (Tollefsen and Buen, 2022). Between September and November 2019, across all hydrophones, there was a notable frequency band of baleen whale vocal activity around 20 Hz (Fig. 2c, d). During the recordings, there were periods of near-continuous tonal sounds (with harmonics) below 20 Hz, attributed to flow noise (Fig. 2f). This phenomenon was compared to time series data for hydrostatic pressure along the hydrophone moorings (presented and discussed in Sec. S7, Fig. S5). While not all periods of increased hydrostatic pressure resulted in these tonal sounds, periods where these sounds were concurrent with increased hydrostatic pressure were attributed to current-driven mooring pull downs (Tan et al., 2025). Some context on what is known about ocean currents in the region is given in Section S6 and S7. NERSC1 was least affected by flow noise, likely due to a different flotation device used, with mid-May 2020 being the only time with sustained self-noise (Fig. 7a).

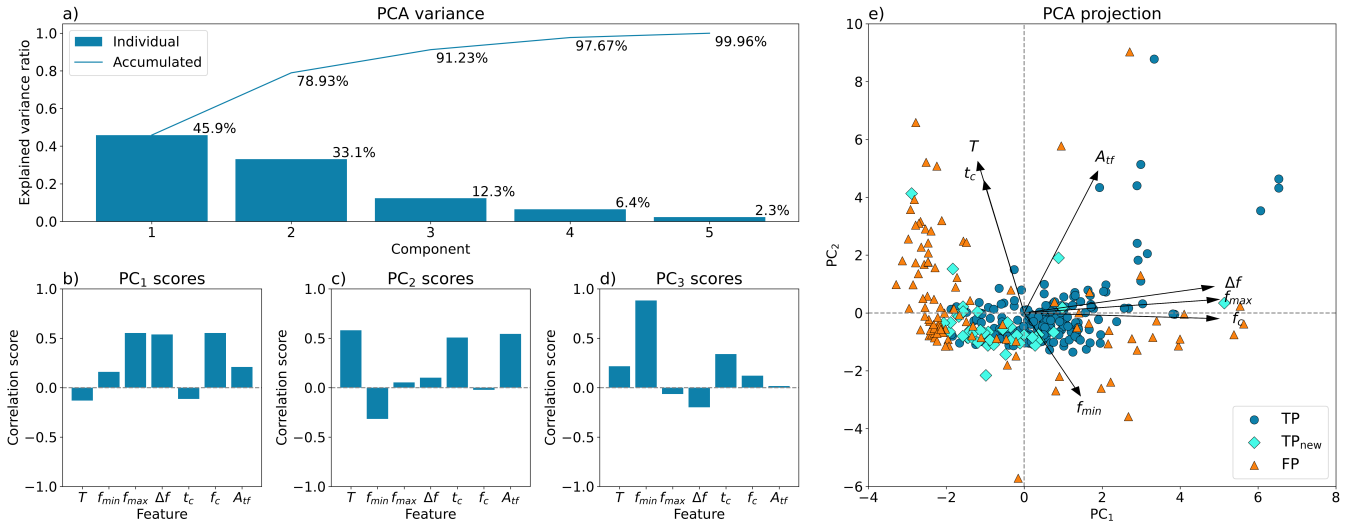


Figure 5 Findings from PCA of ROI acoustic features. a) Explained variance of each component, with accumulated variance. b-d) Plots of correlation scores of acoustic features for the first three principal components. e) 2D projection of the first principal component against the second, with the influence of each acoustic feature represented by arrows. Blue circles, teal diamonds and orange triangles represent True Positive seismic detections (TP), newly discovered seismic detections (TP_{new}) and False Positive detections (FP) respectively.

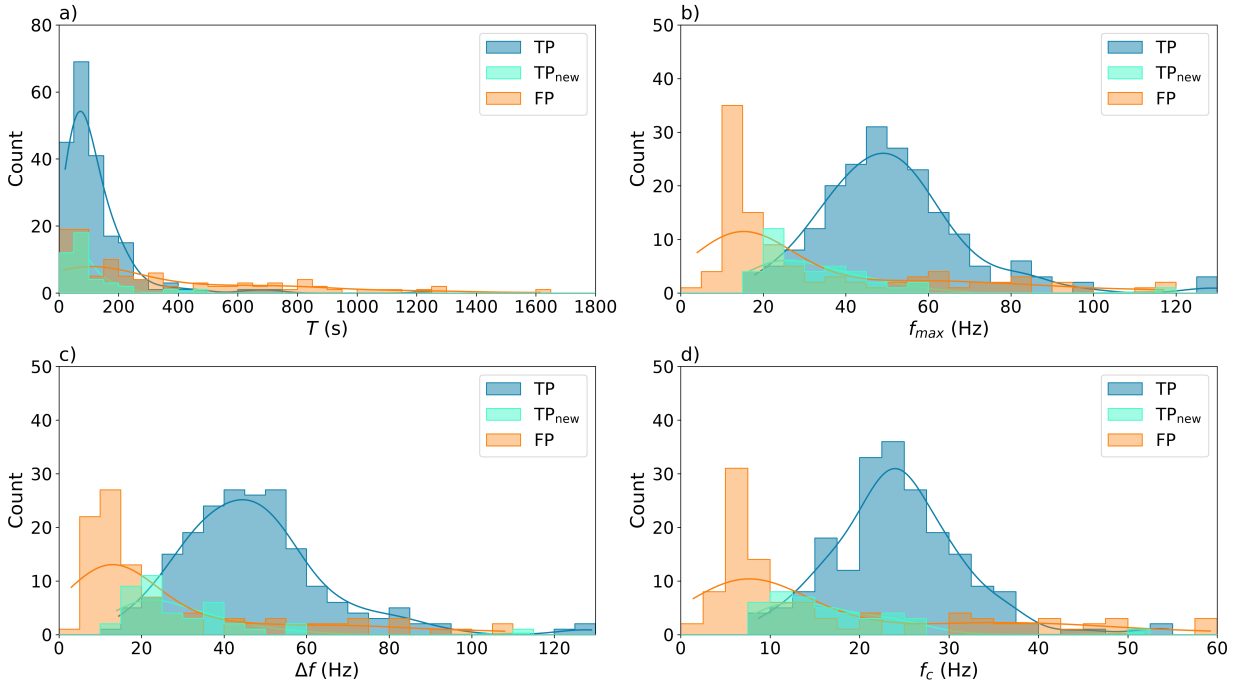


Figure 6 Histograms comparing the acoustic feature distributions for True Positive seismic detections (TP, blue), newly discovered seismic detections (TP_{new}, teal) and False Positive detections (FP, orange): a) duration, T, b) maximum frequency, f_{max}, c) bandwidth, Δf, and d) centroid frequency, f_c. Lines represent probability density functions for the distributions. Note that panel d) has a more restricted frequency range than panels b) and c), as computed ROIs with $f_c > 60$ Hz were filtered out as part of the detector procedure.

For NERSC3 and NERSC2, flow noise was more common between January and June 2020, raising noise levels considerably between 2 Hz and 20 Hz (Fig. 7c and e).

Weekly counts of True Positives, False Positives and False Negatives were compared to the variations in background noise across the dataset (Fig. 7b, d and f). Manually detected seismic signals were more concentrated towards the first five months of the deployment (60 out of 96 occurring before February 2020), with counts of True Positives being higher during this period across all hydrophones. False Negative counts did not appear to have any correlation with increased background noise levels; rather, signals were missed largely due to their signal quality. Flow noise affected the detection performance for Weak signals, such as Event 59 being missed by the detector at NERSC2 due to flow noise producing higher PSD levels. Event 68 was captured at NERSC3, but the earthquake signature was concur-

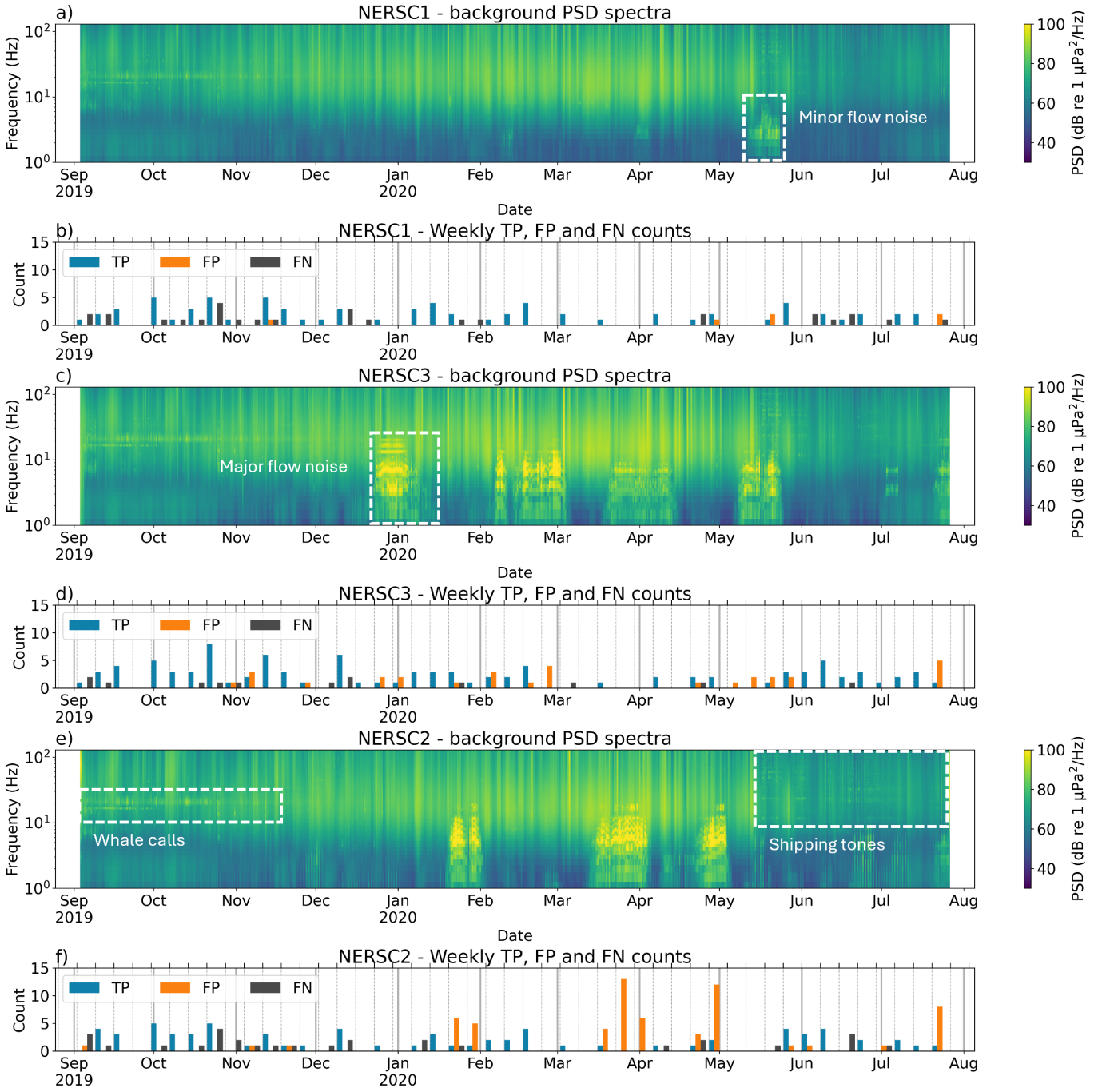


Figure 7 Long-term spectrograms and weekly event counts across deployments at (a-b) NERSC1, (c-d) NERSC3 and (e-f) NERSC2. The 95th-percentile PSD spectra of each recording are presented along the spectrograms, with any parts occupied by an ROI omitted. Weekly counts of True Positives (TP and seismic activity discovered by the detector, TP_{new}), False Positives (FP) and False Negatives (FN) are presented here to allow for more direct comparisons with background noise levels across the dataset.

rent with flow noise, resulting in the two phenomena combining into a 1200-s long ROI. Intermittent sounds from sea ice or marine mammals were effectively suppressed during the pre-processing stages of the ROI detector; hence, they did not influence its performance.

The main causes for False Positive detections have been summarised in Table S1. False Positive counts vary dramatically between hydrophones, with very few instances at NERSC1 (Fig. 7b) compared to NERSC3 and NERSC2 (Fig. 7d and f). Many of the False Positives occurred during weeks when flow noise was present, with at least 66 out of the 100 False Positives resulting from segments of the flow noise being picked up by the detector. ROIs comprising flow noise were characterised by low spectral and, at times, extended temporal acoustic features. The next most common cause for False Positive detections, linked to 20 instances, was due to intermittent low-frequency tones (again < 20 Hz), accompanied by many harmonics. These signals were more complex than the tonal flow noise, and while generally rare during the deployment of CAATEX, this phenomenon was observable at all hydrophones when present. These unidentified sounds dominated recordings during the last few days of the deployment (23rd to

26th July 2020). For the remaining False Positive detections, only one has a verifiable sound, caused by a brief increase in background noise, which can occur during wind-sea ice interactions.

Differences in the PSD spectra for background noise and ROIs were compared, as summarised in the empirical probability density (EPD) plots in Figure 8. A comparison of background noise spectra across the CAATEX moorings and previous measurements of ambient noise across the Nansen Basin by Ozanich et al. (2017) is presented in Section S8 and Figure S6. Background noise (Fig. 8a) was largely stable when only natural sources were present, with a broad peak at 20 Hz. The presence of flow noise introduced increased low-frequency content peaking between 5 and 8 Hz. The spectra within True Positive ROIs are uniform, with a peak typically centred between 10 and 30 Hz (Fig. 8b), with increases in received level of up to 50 dB for the strongest signal. Most of the acoustic energy of seismic activity was contained within the 3 to 50 Hz frequency band, although some of the stronger signals resulted in increased levels across higher frequencies. When observing False Positive ROIs spectra (Fig. 8c), the prevalence of flow noise artefacts being captured within ROIs is highlighted well, with an increase in EPD at the 5 to 8 Hz peak shared with the background noise spectra. Above 10 Hz, PSD levels within False Positive ROIs resemble that of background noise, suggesting that even if the frequency extents of ROIs were extended during computation, the majority of acoustic energy was focussed below 10 Hz for most occasions. For ROIs associated with unannotated seismic activity (Fig. 8d), the peak in PSD is less pronounced, as this activity was generally weaker than the majority of annotated events. The average centre frequency of unannotated seismic ROIs dropped down to between 10 and 15 Hz when compared to ROIs associated with annotated seismic signals.

4.6 Received Level of T-phase signals and comparisons to land station data

Maximum Received Levels (RL_{max}) were measured within the spectro-temporal bounds of each ROI associated with True Positive detections and newly discovered activity. Boxplots of RL_{max} values per hydrophone are presented in Figure 9, with True Positive detections split further by their signal qualities (Sec. 3.2 and 4.1). Generally, RL_{max} measurements align with the signal qualities determined during the manual annotation stage. There is overlap in values across qualities in part due to visibility of T-phase signal in the spectrogram, be it obscured by background noise or flow noise, affecting the manual annotation process. Note that the high-pass filter applied during the recording of CAATEX (Sec. 3.1) has likely led to slight underestimates of RL_{max} as energy from seismic signals below 7 Hz would have been suppressed.

For True Positive detections, RL_{max} was on average highest at NERSC3 across all signal qualities. At NERSC2, where T-phase signals were often labelled with a diminished signal quality compared to the corresponding event at NERSC1 and NERSC3, RL_{max} values still cover the same range of values, with a notably wider range for 'Medium' signal qualities. Interestingly, despite there being fewer 'Strong' signals at NERSC2, the range of RL_{max} values was comparable to NERSC3. There were 6 occasions where RL_{max} for 'Strong' T-phase signals exceeded 130 dB re 1 µPa. These were associated with Events 52 (RL_{max} = 135.1 dB re 1 µPa at NERSC1) and 89 (RL_{max} = 140.8 dB re 1 µPa at NERSC3).

For newly discovered seismic activity, the range of RL_{max} values across hydrophones was significantly different. At NERSC1, which had the fewest number of newly discovered seismic ROIs, the majority of RL_{max} values were within a narrow range of 101 to 106 dB re 1 µPa. RL_{max} values were notably varied at NERSC2, ranging from 95 to 123 dB re 1 µPa. Nonetheless, across hydrophones, the majority of newly discovered ROIs shared similar RL_{max} values to the 'Weak' at the respective hydrophone. With the amplitude thresholds selected for this study, the lowest RL_{max} for a seismic signal was 94.7 dB re 1 µPa, associated with a newly discovered seismic ROI at NERSC1.

5 Discussion and conclusion

Across the manual dataset, 85% of the annotated earthquake events recorded during the CAATEX experiment were successfully detected by the ROI algorithm from at least one hydrophone. Detection performance varied among the three hydrophone moorings mainly due to the quality of the observed T-phase signals. Seismic activity was best recalled at NERSC3, where most labelled T-phase signals were identified as ROIs. More T-phase signals were missed at NERSC1 despite similar signal quality to NERSC3, while NERSC2 received attenuated signals that made some T-phases undetectable even by manual inspection. When comparing the performance of the ROI algorithm, the highest precision was notably achieved at NERSC1, with fewer False Positive detections than NERSC2 and NERSC3. This was due to noise conditions, particularly below 20 Hz, being lower at NERSC1. Across all three hydrophones, nearly all annotated T-phase signals missed by the algorithm (False Negatives) were characterised as having weak signal quality during the annotation stage (excluding one of medium quality). Interestingly, the phase type found in both manual and automatic methods depended on signal quality. The majority of the weak earthquakes featured only the T-phase, whereas stronger earthquakes would commonly feature both the P- and T-phases, hence labelled as P_T signals. Strong and Weak quality signals differed in their amplitude maximum values by around 10 dB re 1 µPa^2/Hz, affecting which phase types were detectable. The capability of multiphase detection (P_T) is an indirect, yet interesting outcome of the ROI algorithm. While T-phases remain the most common phase type recorded (Dziak et al., 2004; Okal, 2008; Ingale et al., 2025), moored hydrophones can also detect solid-earth P-phase converted into hydroacoustic phases (Dziak et al., 2004; Sohn and Hildebrand, 2001; Pulli and Upton, 2002). To our knowledge, the relationship between signal quality (strength) and the observability of earthquake body phases in spectrograms has

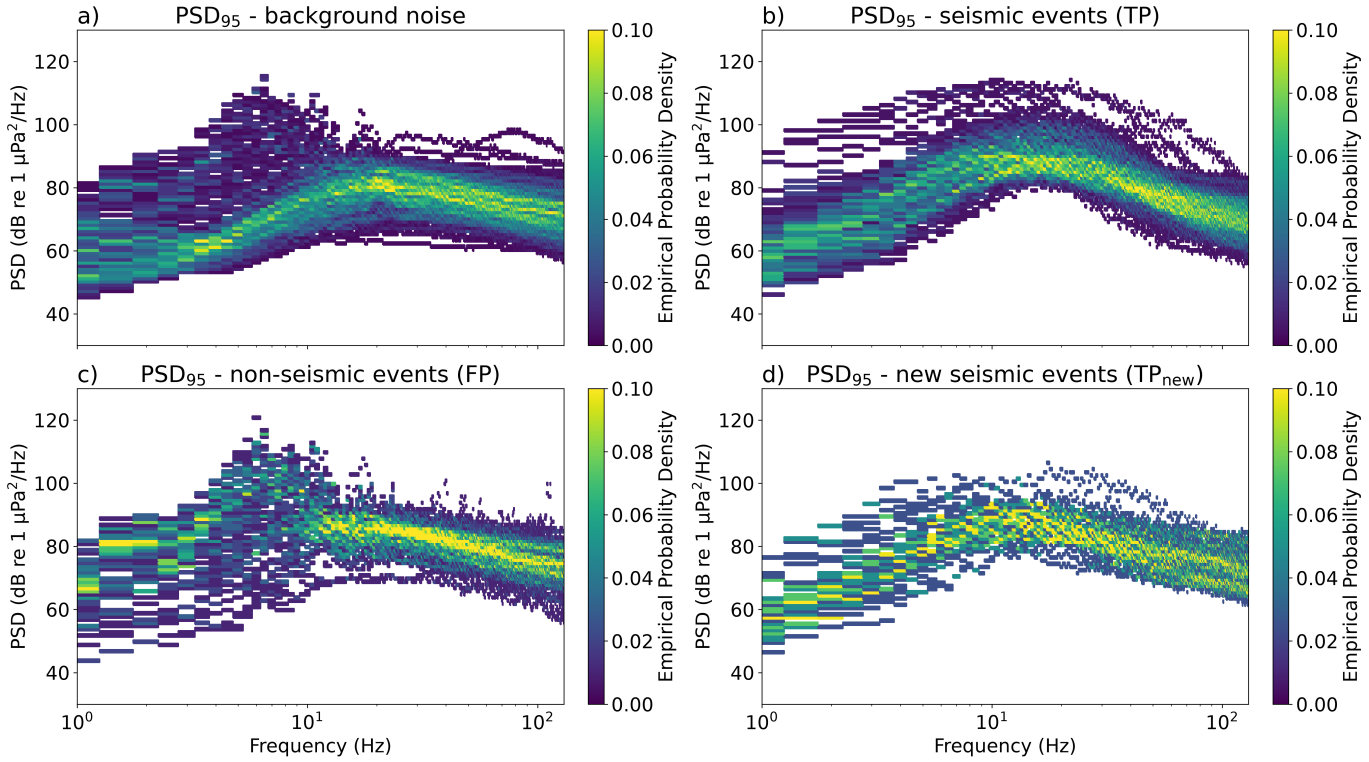


Figure 8 Empirical probability density plots (EPD) of the 95th percentile PSD spectra (PSD_{95}) across all hydrophones. PSD_{95} values (y-axis) are plotted on a set of histograms along the frequency axis (x-axis) to describe the recordings statistically. a) Background noise spectra, taken from sections of the recordings which lie outside the temporal bounds of ROIs. b) Spectra of seismic ROI detections (True Positives, TP). c) Spectra of non-seismic ROI detections (False Positives, FP). d) Spectra of newly discovered seismic activity identified as ROIs (TP_{new}).

not been explored in previous studies.

The algorithm was able to identify additional seismic activity that was not found during the manual annotation stage. These occurrences were characterised by weak signal quality and were mainly recorded in NERSC3 and NERSC2, which may have resulted from manual annotation being completed only on NERSC1. This highlights two interesting aspects of the study. The first is that annotating acoustic datasets can be a time-consuming part of analysis; the ROI algorithm can be used to identify T-phases across unlabelled recordings, thereby assisting the annotation process, provided that the signals are above the amplitude thresholds used. The second aspect relates to the nuanced seismic activity in the Nansen Basin. Despite the three hydrophones being in fairly close proximity to each other, there were several occasions where T-phase signals would be received at some hydrophones but not others, and also instances of the T-phase signals associated with one earthquake appearing with different envelopes across hydrophones. Thus, the direct link between True Positive ROI detections (TP) and the newly discovered seismic activity (TP_{new}) should be carefully interpreted. It is known that T-phase signals can split into multiple signals during propagation, particularly due to reflections off the seafloor, sea surface or underside of sea ice; as such, the same T-phase may present multiple arrivals recorded by the hydrophone (Pulli and Upton, 2002).

Beyond event detection, the ROI algorithm's analysis of the temporal and spectral characteristics of seismic signals highlighted clear differences between True Positive and False Positive detections and provided additional evidence supporting the seismic activity identified. From the PCA analysis, the spectral features (maximum frequency, bandwidth and spectral centroid) contributed the most to explaining variance in the dataset, disentangling the majority of False Positives (mainly from flow noise) from True Positives. It is also visible in the PCA projection how the unlabelled seismic ROIs diverged from the False Positives, albeit with some overlaps and outliers. This aspect is also noticeable when observing distributions of the spectral features. Unlabelled seismic ROIs were mainly characterised by narrower bandwidth in comparison to True Positive detections. Despite that, analysis of Power Spectral Density confirmed how True Positive detections were clearly characterised by having their energy included mainly between 3 and 50 Hz, peaking between 10 and 30 Hz, accordingly with previous studies of T-phases (Fox et al., 2001; Bohnenstiehl et al., 2002; Okal, 2008). Stronger signals had a higher f_{max} as a result of high-frequency components of the signal being well retained during propagation. This can also be seen in observations of maximum Received Levels measured within seismic-related ROIs. Signal quality labels assigned during the annotation stage, while partly dependent on visibility of T-phase signals against background noise, generally correlated with Received Levels. The highest values of Received Levels encountered were all belonging to 'Strong' T-phase signals. New seismic signals discovered by the algorithm had Received Levels largely comparable to 'Weak' True Positive detections. The high-

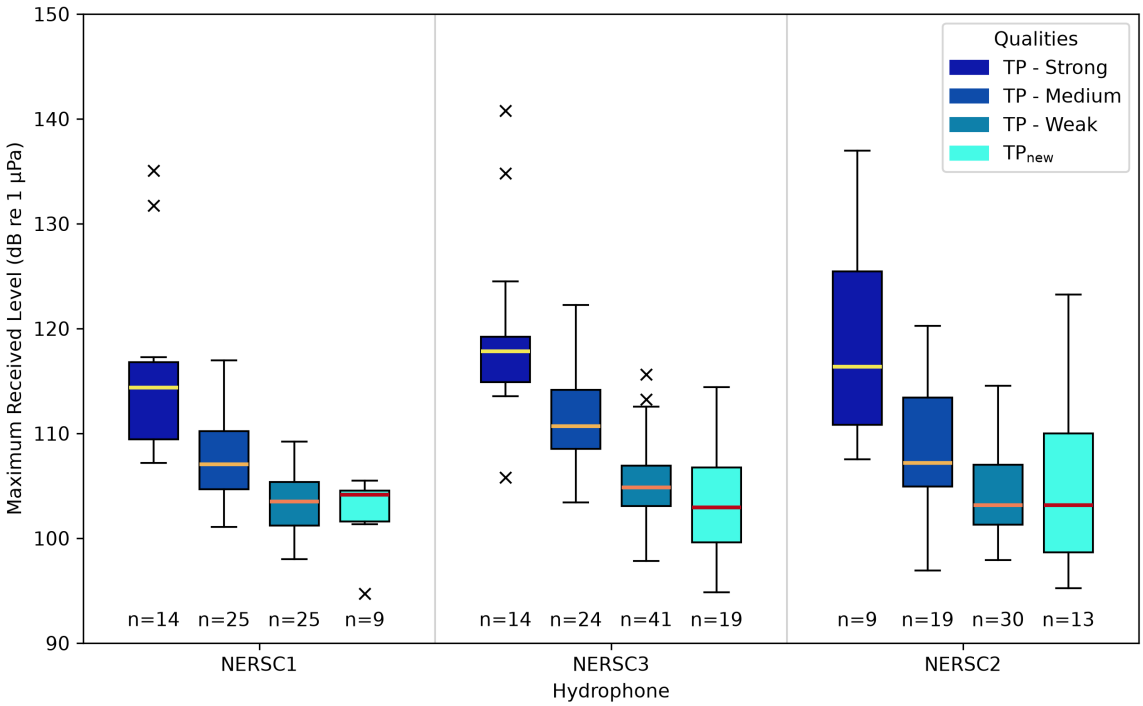


Figure 9 Boxplots of maximum Received Level measured within the temporal and spectral bounds of ROIs. Boxplots represent the True Positive (TP) detections separated by hydrophone (ordered northernmost to southernmost), then separated further by signal quality (deduced during the manual annotation of seismic signals, see Sec. 3.2 and 4.1). Seismic activity discovered by the ROI algorithm (TP_{new}) is represented with an additional boxplot per hydrophone. Box limits contain the 25th to 75th percentiles of Received Level values, with the horizontal line representing the median. Whiskers are placed at data points closest to 1.5 × IQR (interquartile range) above and below the box limits. Outlying values from the whisker ranges are represented by crosses ('x'). The number of ROIs included in each boxplot, taken from Tables 1 and 2, are also given.

pass filter at 7 Hz applied during the original recording of data for CAATEX partly limits analyses of amplitude of received seismic signals. Still, the results of this study demonstrate how the ROI algorithm can be utilised to calculate Received Levels of seismic signals.

When comparing the findings of the current hydroacoustic study to the earthquakes detected from the NNSN land Station network, notable differences in the activity recorded were observed. When considering the 16 earthquakes observed by land stations during the active recording periods of CAATEX, only 5 events were observable (from visual inspection of spectrograms) in the hydrophone recordings from CAATEX. Out of these earthquake events observed using both methods, only 3 had associated Event IDs: Events 52 and 89, the T-phases of which had the highest Received Levels observed; and Event 79, which was observed as a weak signal (maximum Received Level of 107 dB re 1 µPa) despite being recorded as a 4.0 magnitude earthquake at the land stations. The remaining two earthquakes had associated T-phase signals, but these were discovered by the ROI algorithm at NERSC2 and NERSC3, and were not observed at NERSC1. A summary of earthquakes observed by the NNSN land station network, along with details of associated T-phase signals, when applicable, is given in Section S5 and Table S2. It should be noted that, aside from Events 52 and 89, the other 14 earthquakes observed by the land stations were distributed in the Fram Strait (Fig. 1). Given that some earthquakes (Event 79 and the two events with unlabelled seismic ROIs) originated from this region and were observed by the CAATEX hydrophones, there are several possible explanations for why the other earthquakes may have been missed by the hydrophones. The detectability of T-phase signals is dependent on how efficiently they are generated (Bottero et al., 2020), along with the complexity of the ocean structure in the region (Sec. S6; Fig. S4). The Arctic Ocean is distinguished by a shallow sound speed minimum (Diachok, 1976; Sagen et al., 2016, 2017; Hope et al., 2017; Worcester et al., 2020), leading to T-phases experiencing more complex propagation paths (Sohn and Hildebrand, 2001; Blackman et al., 2000; Schlindwein et al., 2005) than what occurs along the SOFAR channel in mid-latitude ocean waters (Ingale et al., 2025; Fox et al., 2001; Dziak et al., 2004). It is worth considering that other factors, such as fault mechanism, source depth, seabed properties, and local bathymetric features (seafloor slopes and topography), can influence how efficiently seismic energy couples into the water, hence affecting the detectability of T-phase signals of a given earthquake (de Groot-Hedlin and Orcutt, 2001; Okal, 2008; Lin et al., 2014; Bottero et al., 2020; de Melo et al., 2021; Takemura et al., 2024).

The algorithm and its preprocessing steps were op-

timised for detecting T-phase signals within a complex Arctic underwater soundscape. Thus, a compromise had to be made between limiting the number of False Positives and False Negatives. The weakest earthquake signals would appear on spectrograms with shorter durations and narrower bandwidths, with amplitudes only just above background noise levels, so they were not sufficiently retained during preprocessing. With the current procedure, the weakest seismic signal that was identified by the ROI algorithm had Received Levels of 94.7 dB re 1 µPa. T-phase signals of duration < 5 s and bandwidth < 2.5 Hz, within the kernel size of the Gaussian filter applied to spectrograms, may have been partly erased from spectrograms during the pre-processing stages, but this was not the reason why any labelled T-phase signals were missed by the algorithm. The high-pass filter applied during recording would have also suppressed seismic signal components below 7 Hz, which may have impeded the algorithm in identifying weaker signals. Currently, earthquake magnitudes cannot be derived from the ROI dataset, as the locations of the earthquakes recorded by hydrophones but not by the land stations remain unknown. Moreover, without the source-receiver distance, it is not possible to calculate a precise Source Level to correlate it with magnitude. This aspect will be the subject of future studies.

Nevertheless, these pre-processing steps were effective in removing short, non-seismic sounds from the spectrogram, as there were no instances of biophony, such as the 20-Hz baleen whale calls (Vacquié-Garcia et al., 2017; Duengen et al., 2022), or discrete cryophonic sounds (crack transients or tones), withstanding the smoothing step and being processed as an ROI. Some cryophonic sounds, mainly increases in background noise due to wind-ice interaction, were identified as ROIs initially, but then discarded using the < 60 Hz spectral centroid filter (Sec. S10; Fig. S10). The majority of False Positives across the dataset were caused by low-frequency (< 20 Hz) continuous tones, which were associated with flow noise. When present, the noise would often withstand the pre-processing stages of the detector, remaining as a large area of increased PSD along the spectrogram, and hence falsely detected as an ROI. Identification of this phenomenon as flow noise was supported by measurements of hydrostatic pressure at the CAATEX moorings (Sec.S7; Fig. S5). While it is beyond the scope of this study to further explore the mechanism responsible for this noise, its presence was linked to periods of increased hydrostatic pressure likely due to mooring pull-downs driven by the ocean currents. An adaptive filter may be considered to remove the flow noise, but further work would be needed to characterise its frequency content (including harmonics) against hydrostatic pressures and current speeds. Aside from one False Positive linked to a brief increase in background noise, the sources of the remaining False Positives have yet to be identified fully, and may be either external sounds or mooring related.

Overall, when compared to existing methods, the key strengths of the ROI algorithm are the ability to identify seismic signals against a variety of environmental noise conditions, as well as extracting spectral characteristics of the signal, which cannot be obtained with temporal-based detectors. Despite the wide usage of STA/LTA (Short-Term-Average/Long-Term-Average) and template matching for detecting seismic signals, both methods present some limitations. STA/LTA works well for impulsive arrivals with a high signal-to-noise ratio, but it can fail to detect weak earthquakes and performs poorly in complex noise conditions (Vaezi and van der Baan, 2015; Yoon et al., 2015). Template matching mainly identifies repeated signals matching a specific waveform, reducing its general applicability. As an alternative, the ROI algorithm presented in this work shows robustness in handling a large variety of T-phase signatures (from impulsive broadband short transients to long-lasting spindle-shaped phases) once the spectrogram has been de-noised using simple preprocessing techniques. An innovative aspect of the algorithm is that it employs few parameters: the kernel size of the Gaussian filter and two amplitude thresholds, allowing greater flexibility in its applicability and the potential to identify previously undetected seismic activity.

While using a manually labelled catalogue as a ground truth may have some inherent limitations, the ROI algorithm is not constrained by a specific dataset characterising only a certain seismic signal type. Moreover, the dataset created to test the detection performance was compiled by a single human expert (MA), thereby reducing the potential label ambiguity and inter-annotator disagreement that could occur when multiple annotators label datasets (Raumer et al., 2024b). One limitation of spectrogram-based detectors is the lack of accuracy for seismic phase arrival. So far, due to the reduced time resolution in spectrograms (1 s set in the current work), the ROI algorithm cannot be used for phase-picking and, in turn, for event location. The detections made by the algorithm, however, can be used to compute signal envelopes, to determine the time of arrival of T-phases and locate the triggering event.

For monitoring seismic activity with T-phase signals recorded by hydrophones, Matsumoto et al. (2006) described a time-domain detection algorithm. Although the processing of real-time datasets is attractive, the detector found a high number of False Positives (52%) and False Negatives (25%), mainly due to the impact of diverse sound environmental conditions. Although studies exploring ML methods for detection of seismic events in seismometer data have been published (reviewed in Kubo et al., 2024), fewer works reported the use of ML tools for T-phase detections from hydroacoustic data (Sukhovich et al., 2014; Raumer et al., 2024b). Overall, whilst promising results have been obtained, ML methods remain computationally demanding, with outcomes difficult to interpret (Guidotti et al., 2018). An initial limitation for ML detectors is their sensitivity to the input data. An explicative example comes from the work of Sukhovich et al. (2014), where an STA/LTA trigger was used to detect P- and T-phases as the first step. Afterwards, identification of seismic signatures was completed using an ML tool trained on a subset of collected signals (i.e. T-phases, P-phases, ship-

generated sound, and iceberg sounds). Limitations may be present in both steps; the use of only STA/LTA for detection may miss signals, and the applicability of the ML tool is constrained to the specific environmental noise conditions encountered. In contrast, the ROI algorithm is user-friendly, featuring only a few parameters and modular steps which can be replaced (e.g. different approaches for noise removal).

To test how the ROI algorithm would perform under different soundscape contexts in detecting regional and teleseismic earthquakes, the benchmarking datasets presented by Raumer et al. (2024a) were used for this purpose. Hydroacoustic datasets from HYDROMOMAR (mid-Atlantic Ocean) and OHASISBIO (southern Indian Ocean) were considered, both available publicly on IFREMER's data store. All 82 of the manually annotated T-phase signals across these two datasets were successfully identified by the ROI algorithm, without adding any changes to the procedure or parameters (i.e., amplitude thresholds) presented in the current work. A summary of results for this benchmarking test is given in Section S9 and Figures S7-9. The use of additional filters or cluster analysis could, however, be recommended to disregard unwanted ROIs when they arise and improve the overall detector performance.

This study presents a 'proof of concept' of detecting microseismic signals in hydroacoustic data using an ROI algorithm as a standalone detector, using recordings from the Nansen Basin. Focus has been placed on observing the T-phase of seismic signals, which were manually labelled by an expert annotator and summarised in a test dataset. The detector performs comparably well to the manual annotator, quantifying temporal and spectral features and offers an opportunity to discover new seismic activity that was neither recorded by the land stations nor manually annotated in the hydrophone datasets. The ROI detector has applications in the preliminary screening of recordings, providing a consistent automated procedure to accelerate annotation of datasets with minimal assumptions about the characteristics of incoming seismic signals. Further, the ROI detector can strengthen ML techniques to define a classifier for seismic activity, using either acoustic features or the signal itself as training data. This combination of techniques highlights a robust solution to further explore earthquake properties generating T-phase signals, particularly for remote regions with diverse seismic activity.

Acknowledgements

The authors thank Prof. Sara Bazin and an anonymous reviewer for their helpful comments and suggestions, and the Seismica editor, Dr. Kenneth Macpherson, for their correspondence. The authors are also grateful to IFREMER for granting access to the benchmark datasets and to Dr. Pierre-Yves Raumer for providing the hydrophone calibration values. The authors also thank the engineers of the Woods Hole Oceanographic Institute and the Scripps Institute of Oceanography, and the crew of the Norwegian Coast Guard vessel Svalbard for their assistance with the moorings. The CAATEX dataset processed in this paper is used with permission from Principal Investigators of the CAATEX projects: Dr. Hanne Sagen, NERSC, (Project No. 280531), funded by the Research Council of Norway, and Dr. Matthew Dzieciuch, Scripps Institution of Oceanography, University of California (Project No. N00014-18-1-2698), funded by the Office of Naval Research (USA). This work was carried out as part of the HiAOOS project funded by the European Union Horizon Europe Programme (Grant Agreement No. 101094621); Mr. Jonathan Cleverly and Prof. Philippe Blondel were supported by UKRI Grant No. 10071903). Views and opinions expressed are, however, are those of the author(s) only and do not necessarily reflect those of the European Union, which cannot be held responsible for them. This work has been completed as part of Mr. Jonathan Cleverly's EPSRC-funded PhD studentship (EP/W524712/1), supervised by Prof. Philippe Blondel.

Data and code availability

The Python scripts and the dataset .csv file used to generate the results may be found on Zenodo at https://doi.org/10.5281/zenodo.17939966. Within the same link are included: a README file explains how to install the relevant Python code for the analyses, the test dataset of the manually labelled T-phases and the dataset of the seismic events used for the map in Figure 1. The locations of these seismic events have been obtained from the Norwegian National Seismic Network (NNSN) at https://nnsn.geo.uib.no/nnsn/#/ and at the International Seismological Centre (ISC) at https://www.isc.ac.uk/. Data on bathymetry can be downloaded at https://www.gebco.net/data-products/gridded-bathymetry-data/arctic-ocean.. All oceanographic data, including hydrostatic pressure, will be made available and accessible when Dundas et al. (2026, in prep.) is published.

Competing interests

The authors declare no competing interests of any type regarding this work.

References

Ainslie, M. A., Robinson, S. P., Harris, P. M., Tyack, P. L., Halvorsen, M. B., Cheong, S.-H., Livina, V., and Wang, L. S. Ocean soundscapes and trends from 2003 to 2021: 10–100 Hz. *The Journal of the Acoustical Society of America*, 157(6):4358–4384, 2025. doi: 10.1121/10.0036831.

Allen, R. V. Automatic earthquake recognition and timing from single traces. *Bulletin of the Seismological Society of America*, 68(5): 1521–1532, 1978. doi: 10.1785/BSSA0680051521.

Bazin, S., Royer, J.-Y., Dubost, F., Paquet, F., Loubrieu, B., Lavayssière, A., Deplus, C., Feuillet, N., Jacques, É., Rinnert, E., and Thinon, I. Initial results from a hydroacoustic network to monitor submarine lava flows near Mayotte Island. *Comptes Rendus. Géoscience*, 354(S2):257–273, 2022. doi: 10.5802/crgeos.119.

Blackman, D. K., Nishimura, C. E., and Orcutt, J. A. Seismoacoustic recordings of a spreading episode on the Mohns Ridge. *Jour-*

nal of Geophysical Research: Solid Earth, 105(B5):10961–10973, 2000. doi: 10.1029/2000JB900011.

Bohnenstiehl, D., Tolstoy, M., Dziak, R., Fox, C., and Smith, D. Aftershock sequences in the mid-ocean ridge environment: An analysis using hydroacoustic data. *Tectonophysics*, 354(1-2):49–70, 2002. doi: 10.1016/S0040-1951(02)00289-5.

Bottero, A., Cristini, P., and Komatitsch, D. On the Influence of Slopes, Source, Seabed and Water Column Properties on T Waves: Generation at Shore. *Pure and Applied Geophysics*, 177: 5695–5711, 2020. doi: 10.1007/s00024-020-02611-z.

Buckingham, M. J. On acoustic transmission in ocean-surface waveguides. *Philosophical Transactions of the Royal Society of London. Series A: Physical and Engineering Sciences*, 335(1639): 513–555, 1991. doi: 10.1098/rsta.1991.0059.

Canny, J. A Computational Approach to Edge Detection. *IEEE Transactions on Pattern Analysis and Machine Intelligence*, PAMI-8(6):679–698, 1986. doi: 10.1109/TPAMI.1986.4767851.

Cleverly, J., Blondel, P., Sagen, H., Dzieciuch, M., and Storheim, E. Automatic identification of biophonics and sea ice processes in large datasets from the High Arcticing Ocean. *Proceedings from the International Conference on Underwater Acoustics 2024 (ICUA2024), Bath, United Kingdom*, 2024. doi: 10.25144/22225.

de Groot-Hedlin, C. D. and Orcutt, J. A. Excitation of T-phases by seafloor scattering. *The Journal of the Acoustical Society of America*, 109(5):1944–1954, 2001. doi: 10.1121/1.1361057.

de Groot-Hedlin, C. D. and Orcutt, J. A. Synthesis of earthquake-generated T-waves. *Geophysical Research Letters*, 26(9): 1227–1230, May 1999. doi: 10.1029/1999GL900205.

de Melo, G. W. S., Parnell-Turner, R., Dziak, R. P., Smith, D. K., Maia, M., do Nascimento, A. F., and Royer, J.-Y. Uppermost Mantle Velocity beneath the Mid-Atlantic Ridge and Transform Faults in the Equatorial Atlantic Ocean. *Bulletin of the Seismological Society of America*, 111(2):1067–1079, 2021. doi: 10.1785/0120200248.

Diachok, O. I. Effects of sea-ice ridges on sound propagation in the Arctic Ocean. *The Journal of the Acoustical Society of America*, 59(5):1110–1120, 1976. doi: 10.1121/1.380965.

Duengen, D., Burkhardt, E., and El-Gabbas, A. Fin whale (Balaenoptera physalus) distribution modeling on their Nordic and Barents Seas feeding grounds. *Marine Mammal Science*, 38(4): 1583–1608, 2022. doi: 10.1111/mms.12943.

Dundas, V., Sagen, H., Beszczynska-Möller, A., Colosi, J., Dzieciuch, M. A., and F., W. P. Northward spreading of Atlantic Water into the Nansen Basin inferred from mooring observations. *in prep.*, 2026.

Dziak, R. P., Bohnenstiehl, D. R., Matsumoto, H., Fox, C. G., Smith, D. K., Tolstoy, M., Lau, T.-K., Haxel, J. H., and Fowler, M. J. P- and T-Wave Detection Thresholds, Pn Velocity Estimate, and Detection of Lower Mantle and Core P-Waves on Ocean Sound-Channel Hydrophones at the Mid-Atlantic Ridge. *Bulletin of the Seismological Society of America*, 94(2):665–677, 2004. doi: 10.1785/0120030156.

Dzieciuch, M., Sagen, H., Worcester, P. F., Storheim, E., Akins, F. H., Sandven, S., Colosi, J. A., Kemp, J. N., and Leinebø, G. M. Transarctic acoustic transmissions during the Coordinated Arctic Acoustic Thermometry Experiment in 2019–2020. *The Journal of the Acoustical Society of America*, 159:1071–1085, 2026. doi: 10.1121/10.0042233.

Dzieciuch, M. A., Sagen, H., Worcester, P. F., Storheim, E., Colosi, J. A., Krishfield, R. A., Sandven, S., and Geyer, F. The coordinated arctic acoustic thermometry experiment - CAATEX. *The Journal of the Acoustical Society of America*, 152:A72, 2022. doi: 10.1121/10.0015587.

Escobar-Amado, C., Badiey, M., and Pecknold, S. Automatic detection and classification of bearded seal vocalizations in the northeastern Chukchi Sea using convolutional neural networks. *The Journal of the Acoustical Society of America*, 151(1):299–309, 2022. doi: 10.1121/10.0009256.

Fox, C. G. and Dziak, R. P. Hydroacoustic detection of volcanic activity on the Gorda Ridge, February–March 1996. *Deep Sea Research Part II: Topical Studies in Oceanography*, 45(12): 2513–2530, 1998. doi: 10.1016/S0967-0645(98)00081-2.

Fox, C. G., Matsumoto, H., and Lau, T.-K. A. Monitoring Pacific Ocean seismicity from an autonomous hydrophone array. *Journal of Geophysical Research*, 106(B3):4183–4206, 2001. doi: 10.1029/2000JB900404.

Garibbo, S. *Low Frequency Ocean Acoustic Processes*. PhD thesis, Department of Physics, University of Bath, Bath, United Kingdom, 2023. https://researchportal.bath.ac.uk/en/studentTheses/low-frequency-ocean-acoustic-phenomena/.

Goslin, J., Perrot, J., Royer, J.-Y., Martin, C., Lourenço, N., Luis, J., Dziak, R. P., Matsumoto, H., Haxel, J., Fowler, M. J., Fox, C. G., Lau, A. T.-K., and Bazin, S. Spatiotemporal distribution of the seismicity along the Mid-Atlantic Ridge north of the Azores from hydroacoustic data: Insights into seismogenic processes in a ridge–hot spot context. *Geochemistry, Geophysics, Geosystems*, 13(2), 2012. doi: 10.1029/2011GC003828.

Greenacre, M., Groenen, P. J. F., Hastie, T., D'Enza, A. I., Markos, A., and Tuzhilina, E. Principal component analysis. *Nature Reviews Methods Primers*, 2(100), 2022. doi: 10.1038/s43586-022-00184-w.

Guidotti, R., Monreale, A., Ruggieri, S., Turini, F., Giannotti, F., and Pedreschi, D. A Survey of Methods for Explaining Black Box Models. *ACM computing surveys (CSUR)*, 51(5):1–42, 2018. doi: 10.1145/3236009.

Guilbert, J., Vergoz, J., Schisselé, E., Roueff, A., and Cansi, Y. Use of hydroacoustic and seismic arrays to observe rupture propagation and source extent of the Mw = 9.0 Sumatra earthquake. *Geophysical Research Letters*, 32(15), 2005. doi: 10.1029/2005GL022966.

Hildebrand, J. A. Anthropogenic and natural sources of ambient noise in the ocean. *Marine Ecology Progress Series*, 395:5–20, 2009. doi: 10.3354/meps08353.

Hope, G., Sagen, H., Storheim, E., Hobæk, H., and Freitag, L. Measured and modeled acoustic propagation underneath the rough Arctic sea-ice. *The Journal of the Acoustical Society of America*, 142(3):1619–1633, 2017. doi: 10.1121/1.5003786.

Ingale, V. V., Bazin, S., and Royer, J. Y. Hydroacoustic Observations of Two Contrasted Seismic Swarms along the Southwest Indian Ridge in 2018. *Geosciences*, 11(6):225, 2021. doi: 10.3390/geosciences11060225.

Ingale, V. V., Bazin, S., Olive, J.-A., Briais, A., and Royer, J.-Y. Hydroacoustic Study of a Seismic Swarm in 2016–2017 near the Melville Transform Fault on the Southwest Indian Ridge. *Bulletin of the Seismological Society of America*, 113(4):1523–1541, 2023. doi: 10.1785/0120220213.

Ingale, V. V., Tepp, G., Dziak, R. P., and Parnell-Turner, R. Detection and Analysis of Aleutian Arc Seismicity (2022-2023) Using an Autonomous Hydrophone Array. *Geochemistry, Geophysics, Geosystems*, 26(8), 2025. doi: 10.1029/2025GC012320.

Jakobssen, M., Mohammad, R., Karlsson, M., et al. The International Bathymetric Chart of the Arctic Ocean Version 5.0. *Scientific Data*, 11:1420, 2024. doi: 10.1038/s41597-024-04278-w.

Jamet, G., Guennou, C., Guillon, L., Mazoyer, C., and Royer, J.-Y. T-wave generation and propagation: A comparison between data and spectral element modeling. *The Journal of the Acoustical Society of America*, 134(4):3376–3385, Oct. 2013. doi:

10.1121/1.4818902.

Jeddi, Z., Ottemöller, L., Sørensen, M. B., Rezaei, S., Gibbons, S. J., Strømme, M. L., Voss, P. H., and Dahl-Jensen, T. Improved Seismic Monitoring with OBS Deployment in the Arctic: A Pilot Study from Offshore Western Svalbard. *Seismological Society of America*, 92(5):2705–2717, 2021. doi: 10.1785/0220200471.

Jolliffe, I. T. and Cadima, J. Principal component analysis: a review and recent developments. *Philosophocal Transactions Royal Society A*, 374:20150202, 2016. doi: 10.1098/rsta.2015.0202.

Keenan, R. E. and Merriam, L. R. L. Arctic abyssal *T* phases: Coupling seismic energy to the ocean sound channel via under-ice scattering. *The Journal of the Acoustical Society of America*, 88 (S1):S182–S182, 1990. doi: 10.1121/1.2028815.

Kong, L. S. L., Solomon, S. C., and Purdy, G. M. Microearthquake Characteristics of a Mid-Ocean Ridge along-axis high. *Journal of Geophysical Research: Solid Earth*, 97(B2):1659–1685, 1992. doi: 10.1029/91JB02566.

Koulakov, I., Schlindwein, V., Liu, M., Gerya, T., Jakovlev, A., and Ivanov, A. Low-degree mantle melting controls the deep seismicity and explosive volcanism of the Gakkel Ridge. *Nature Communications*, 13(1):3122, 2022. doi: 10.1038/s41467-022-30797-4.

Kubo, H., Naoi, M., and Kano, M. Recent advances in earthquake seismology using machine learning. *Earth, Planets and Space*, 76(1):36, 2024. doi: 10.1186/s40623-024-01982-0.

Lavayssière, A., Bazin, S., and Royer, J. Y. Hydroacoustic Monitoring of Mayotte Submarine Volcano during Its Eruptive Phase. *Geosciences*, 14(6):170, 2024. doi: 10.3390/geosciences14060170.

Lin, C.-W., Chuang, L. Y.-L., Huang, C.-F., Chen, C.-W., and Kuo, B.-Y. T-wave observations on ocean-bottom seismometers offshore Eastern Taiwan. In *OCEANS 2014-TAIPEI*, pages 1–5. IEEE, 2014. doi: 10.1109/OCEANS-TAIPEI.2014.6964430.

Matsumoto, H., Dziak, R. P., Mellinger, D. K., Fowler, M., Haxel, J., Lau, A., Meinig, C., Bumgardner, J., and Hannah, W. Autonomous hydrophones at NOAA/OSU and a new seafloor sentry system for real-time detection of acoustic events. In *OCEANS 2006 MTS/IEEE Boston. IEEE*, pages 1–4, 2006. doi: 10.1109/OCEANS.2006.307041.

Merchant, N. D., Fristrup, K. M., Johnson, M. P., Tyack, P. L., Witt, M. J., Blondel, P., and Parks, S. E. Measuring acoustic habitats. *Methods in Ecology and Evolution*, 13(4):247–362, 2015. doi: 10.1111/2041-210X.12330.

Munk, W., Worcester, P. F. J. O., and Wunsch, C. *Ocean acoustic tomography*. Cambridge University Press, 1995. doi: 10.1017/CBO9780511666926.

Okal, E. A. The generation of T waves by earthquakes. *Advances in Geophysics*, 49:1–65, 2008. doi: 10.1016/S0065-2687(07)49001-X.

Oliveira, T., Prior, M., Saragiotis, C., Park, J., Metz, D., Bittner, P., Qorbani, E., Khukhuudei, U., and Pérez-Campos, X. Global Detection Capabilities of T Phases Using the IMS Hydrophone Network. *Seismological Research Letters*, 96(2A):731–743, 2025. doi: 10.1785/0220240418.

Ozanich, E., Gerstoft, P., Worcester, P. F., Dzieciuch, M. A., and Thode, A. Eastern Arctic ambient noise on a drifting vertical array. *The Journal of the Acoustical Society of America*, 142(4): 1997–2006, 2017. doi: 10.1121/1.5006053.

Park, M., Odom, R. I., and Soukup, D. J. Modal scattering: A key to understanding oceanic T-waves. *Geophysical Research Letters*, 28(17):3401–3404, Sept. 2001. doi: 10.1029/2001GL013472.

Parnell-Turner, R., Smith, D. K., and Dziak, R. P. Hydroacoustic monitoring of seafloor spreading and transform faulting in the equatorial Atlantic Ocean. *Journal of Geophysical Research: Solid Earth*, 127(7), 2022. doi: 10.1029/2022JB024008.

Pulli, J. J. and Upton, Z. M. Hydroacoustic observations of Indian earthquake provide new data on T-waves. *Eos, Transactions American Geophysical Union*, 83(13):145–151, 2002. doi: 10.1029/2002EO000090.

Raumer, P.-Y., Bazin, S., Cazau, D., Ingale, V. V., and Royer, J.-Y. Données hydro-acoustiques passives 240 Hz annotées en océan Atlantique 2013 et océan Indien Sud 2018 et 2020. *IFREMER*, 2024a. doi: 10.12770/b618b24e-82f9-4b3b-9753-048e1f043ca6.

Raumer, P.-Y., Bazin, S., Cazau, D., Ingale, V. V., Royer, J.-Y., and Lavayssière, A. An Open Source Hydroacoustic Benchmarking Framework for Geophonic Signal Detection. *Seismica*, 3(2): 1344, 2024b. doi: 10.26443/seismica.v3i2.1344.

Rodríguez, O., Duarte, R. J., and Jesus, S. M. PAM2PY: a Python tool for sharing ocean soundscape data. *Proceedings from the 6th Underwater Acoustics Conference and Exhibition 2021 (UACE2021), Virtual*, 2021. doi: 10.1121/2.0001471.

Sagen, H., Dushaw, B. D., Skarsoulis, E. K., Dumont, D., Dzieciuch, M. A., and Beszczynska-Möller, A. Time series of temperature in Fram Strait determined from the 2008–2009 DAMOCLES acoustic tomography measurements and an ocean model. *Journal of Geophysical Research: Oceans*, 121(7):4601–4617, 2016. doi: 10.1002/2015JC011591.

Sagen, H., Worcester, P. F., Dzieciuch, M. A., Geyer, F., Sandven, S., Babiker, M., Beszczynska-Möller, A., Dushaw, B. D., and Cornuelle, B. Resolution, identification, and stability of broadband acoustic arrivals in Fram Strait. *The Journal of the Acoustical Society of America*, 141(3):2055–2068, 2017. doi: 10.1121/1.4978780.

Saurel, J., Retailleau, L., Deplus, C., Loubrieu, B., Pierre, D., Frangieh, M., Khelifi, N., Bonnet, R., Ferrazzini, V., Bazin, S., and Guyavarch, P. Combining hydro-acoustic sources and bathymetric differences to track the vent evolution of the Mayotte eruption, Mozambique Channel. *Frontiers in Earth Science*, 10, 2022. doi: 10.3389/feart.2022.983051.

Schlindwein, V., Müller, C., and Jokat, W. Seismoacoustic evidence for volcanic activity on the ultraslow-spreading Gakkel ridge, Arctic Ocean. *Geophysical Research Letters*, 32(18), 2005. doi: 10.1029/2005GL023767.

Schlindwein, V., Müller, C., and Jokat, W. Microseismicity of the ultraslow-spreading Gakkel Ridge, Arctic Ocean: a pilot study. *Geophysical Journal International*, 169(1):100–112, 2007. doi: 10.1111/j.1365-246X.2006.03308.x.

Schlindwein, V., Li, S., Kirk, H., and Schmidt-Aursch, M. C. Seismic soundscape of the Arctic Ocean: seasonal effects of sea ice and swell on deep-sea ocean bottom seismometer records. *Geophysical Journal International*, 242(1), 2025. doi: 10.1093/gji/ggaf143.

Schreiner, A. E., Fox, C. G., and Dziak, R. P. Spectra and magnitudes of T-waves from the 1993 earthquake swarm on the Juan de Fuca Ridge. *Geophysical research letters*, 22(2):139–142, 1995. doi: 10.1029/94GL01912.

Schwardt, M., Pilger, C., Gaebler, P., P., H., and L., C. Natural and anthropogenic sources of seismic, hydroacoustic, and infrasonic waves: Waveforms and spectral characteristics (and their applicability for sensor calibration). *Surveys in Geophysics*, 43(5): 1265–1361, 2022. doi: 10.1007/s10712-022-09713-4.

Shapiro, L. G. Connected Component Labeling and Adjacency Graph Construction. *Machine Intelligence and Pattern Recognition*, 19:1–30, 1996. doi: 10.1016/S0923-0459(96)80011-5.

Sohn, R. A. and Hildebrand, J. A. Hydroacoustic earthquake detection in the Arctic Basin with the Spinnaker Array. *Bulletin of the Seismological Society of America*, 91(3):572–579, 2001. doi: 10.1785/0120000099.

Sukhovich, A., Irisson, J.-O., Perrot, J., and Nolet, G. Automatic recognition of T and teleseismic P waves by statistical analysis of their spectra: An application to continuous records of moored hydrophones. *Journal of Geophysical Research: Solid Earth*, 119 (8):6469–6485, 2014. doi: 10.1002/2013JB010936.

Takemura, S., Kubota, T., and Sandanbata, O. Successive Tsunamigenic Events Near Sofu Seamount Inferred From High-Frequency Teleseismic P and Regional T Waves. *Journal of Geophysical Research: Solid Earth*, 129(10), 2024. doi: 10.1029/2024JB029746.

Talandier, J. and Okal, E. A. Seismic detection of underwater volcanism: The example of French Polynesia. *Pure and applied Geophysics*, 125(6):919–950, 1987. doi: 10.1007/BF00879361.

Talandier, J. and Okal, E. A. On the mechanism of conversion of seismic waves to and from T waves in the vicinity of island shores. *Bulletin of the Seismological Society of America*, 88(2): 621–632, 1998. doi: 10.1785/BSSA0880020621.

Tan, T., Godin, O. A., Walters, M. W., and Joseph, J. E. Physics-informed and machine learning-enabled retrieval of ocean current speed from flow noise. *The Journal of the Acoustical Society of America*, 157(2):1084–1096, 2025. doi: 10.1121/10.0035800.

Thode, A. M., Kim, K. H., Blackwell, S. B., Greene Jr., C. R., Nations, C. S., McDonald, T. L., and Macrander, A. M. Automated detection and localization of bowhead whale sounds in the presence of seismic airgun surveys. *The Journal of the Acoustical Society of America*, 131(5):3726–3747, 2012. doi: 10.1121/1.3699247.

Tollefsen, D. and Buen, H. Wind- and tidal driven ambient noise in seasonally ice-covered waters north of the Svalbard archipelago. *JASA Express Letters*, 2(8):086001, 2022. doi: 10.1121/10.0013687.

Tolstoy, I. and Ewing, M. The T phase of shallow-focus earthquakes. *Bulletin of the Seismological Society of America*, 40(1): 25–51, 1950. doi: 10.1785/BSSA0400010025.

Tolstoy, M. and Bohnenstiehl, D. R. Hydroacoustic Constraints on the Rupture Duration, Length, and Speed of the Great Sumatra-Andaman Earthquake. *Seismological Research Letters*, 76(4): 419–425, 2005. doi: 10.1785/gssrl.76.4.419.

Ulloa, J., Haupert, S., Latorre, J., Aubin, T., and Sueuer, J. scikit-maad: An opensource and modular toolbox for quantitative soundscape analysis in Python. *Methods in Ecology and Evolution*, 12:2334–2340, 2021. doi: 10.1111/2041-210X.13711.

Vacquié-Garcia, J., Lydersen, C., Marques, T., Aars, J., Ahonen, H., Skern-Mauritzen, M., Øien, N., and Kovacs, K. Late summer distribution and abundance of ice-associated whales in the Norwegian High Arctic. *Endangered Species Research*, 32:59–70, 2017. doi: 10.3354/esr00791.

Vaezi, Y. and van der Baan, M. Comparison of the STA/LTA and power spectral density methods for microseismic event detection. *Geophysical Journal International*, 203(3):1896–1908, 2015. doi: 10.1093/gji/ggv419.

Walker, D. A., McCreery, C. S., and Hiyoshi, Y. T-phase spectra, seismic moments, and tsunamigenesis. *Bulletin of the Seismological Society of America*, 82(3):1275–1305, 1992. doi: 10.1785/BSSA0820031275.

Wiggins, S. M., Roch, M. A., and John A. Hildebrand, J. A. TRITON software package: analyzing large passive acoustic monitoring data sets using MATLAB. *The Journal of the Acoustical Society of America*, 128(4_Supplement):2299–2299, 2010. doi: 10.1121/1.3508074.

Williams, C. M., Stephen, R. A., and Smith, D. K. Hydroacoustic events located at the intersection of the Atlantis $(30^{\circ}\mathrm{N})$ and Kane $(23^{\circ}40'\mathrm{N})$ Transform Faults with the Mid-Atlantic Ridge. *Geochemistry, Geophysics, Geosystems*, 7(6), 2006. doi: 10.1029/2005GC001127.

Withers, M., Aster, R., Young, C., Beiriger, J., Harris, M., Moore, S., and Trujillo, J. A comparison of select trigger algorithms for automated global seismic phase and event detection. *Bulletin of the Seismological Society of America*, 88(1):95–106, 1998. doi: 10.1785/BSSA0880010095.

Wolfe, C. J., Purdy, G. M., Toomey, D. R., and Solomon, S. C. Microearthquake characteristics and crustal velocity structure at 29°N on the Mid-Atlantic Ridge: The architecture of a slow spreading segment. *Journal of Geophysical Research: Solid Earth*, 100(B12):24449–24472, 1995. doi: 10.1029/95JB02399.

Worcester, P., Dzieciuch, M., and Sagen, H. Ocean Acoustics in the Rapidly Changing Arctic. *Acoustics Today*, 16(1):55–64, 2020. doi: 10.1121/AT.2020.16.1.55.

Yang, Y. and Forsyth, D. W. Improving Epicentral and Magnitude Estimation of Earthquakes from T Phases by Considering the Excitation Function. *Bulletin of the Seismological Society of America*, 93(5):2106–2122, Oct. 2003. doi: 10.1785/0120020215.

Yoon, C. E., O'Reilly, O., Bergen, K. J., and Beroza, G. C. Earthquake detection through computationally efficient similarity search. *Science Advances*, 1(11), 2015. doi: 10.1126/sciadv.1501057.

The article *T-phase detection within spectrograms of hydroacoustic data from the Arctic Ocean* © 2026 by Marianna Anichini is licensed under CC BY 4.0.